J. Fluid Mech. (2010), *vol.* 658, *pp.* 33–62.
doi:10.1017/S0022112010001539

Interaction of a deformable free surface with statistically steady homogeneous turbulence

XIN GUO AND LIAN SHEN†

Department of Civil Engineering, Johns Hopkins University, Baltimore, MD 21218, USA

(Received 22 July 2009; revised 23 March 2010; accepted 23 March 2010;
first published online 10 June 2010)

Direct numerical simulation is performed for the interaction between a deformable free surface and the homogeneous isotropic turbulent flow underneath. The Navier–Stokes equations subject to fully nonlinear free-surface boundary conditions are simulated by using a pseudospectral method in the horizontal directions and a finite-difference method in the vertical direction. Statistically, steady turbulence is generated by using a linear forcing method in the bulk flow below. Through investigation of cases of different Froude and Weber numbers, the present study focuses on the effect of surface deformation of finite amplitude. It is found that the motion of the free surface is characterized by propagating waves and turbulence-generated surface roughness. Statistics of the turbulence field near the free surface are analysed in detail in terms of fluctuations of velocity, fluctuations of velocity gradients and strain rates and the energy budget for horizontal and vertical turbulent motions. Our results illustrate the effects of surface blockage and vanishing shear stress on the anisotropy of the flow field. Using conditional averaging analysis, it is shown that splats and antisplats play an essential role in energy inter-component exchange and vertical transport.

1. Introduction

The physics of free-surface turbulence is important to numerous environmental and engineering applications including air–sea exchange of mass, heat and momentum, ship hydrodynamics and remote sensing and many industrial equipments involving gas–liquid flows. The interaction between a free surface and the turbulent flow underneath is a complex process. On one hand, the surface is deformed by the turbulence from below, resulting in surface roughness and waves. On the other hand, the turbulence is subject to the unique constraints of the free surface on the fluid motion, namely the kinematic boundary condition (KBC) requiring that the surface remains material, and the dynamic boundary conditions (DBCs) imposing the stress balance at the free surface. Our understanding of free-surface turbulence is much less than its counterpart of turbulence at a solid wall, and there is a critical need for its study.

Because of its importance, the problem of free-surface turbulence started to receive considerable attention recently in theoretical, numerical and experimental studies. Notably, Hunt & Graham (1978) and Hunt (1984) used the rapid distortion theory to establish a theoretical framework. Two surface layers, an inner viscous layer and an outer source layer, were identified, and the variation of turbulence spectrum near

† Email address for correspondence: lianshen@jhu.edu

the surface was analysed. Teixeira & Belcher (2000) extended the theory of Hunt–Graham to include viscous effect. Turbulence dissipation near the free surface was studied. Magnaudet (2003) showed that at high Reynolds numbers, the theory is still the leading-order approximation for the long-term evolution of the turbulence near a shear-free boundary.

Accompanied by the developments in the theoretical analysis, substantial information on the details of the flow field has been obtained from simulations and measurements. In numerical study, usually three types of flows are simulated: open-channel flow (e.g. Lam & Banerjee 1988; Handler *et al.* 1993; Komori *et al.* 1993; Borue, Orszag & Staroselsky 1995; Hodges & Street 1999; Nagaosa 1999; Nagaosa & Handler 2003), shear flow under a free surface (e.g. Dimas & Triantafyllou 1994; Tsai 1998; Shen *et al.* 1999) and decaying isotropic turbulence with a free-slip plate suddenly inserted (e.g. Perot & Moin 1995; Walker, Leighton & Garza-Rios 1996). For a mechanistic study, these three flows have their advantages and disadvantages. The open-channel flow is statistically steady and it corresponds directly to numerous laboratory measurements (e.g. Rashidi 1997; Kumar, Gupta & Banerjee 1998; Smolentsev & Miraghaie 2005). The effect of the channel bottom is, however, difficult to separate from the dynamics at the free surface, especially when the Reynolds number is not sufficiently large (cf. the discussion of Calmet & Magnaudet 2003). The shear flow provides many theoretical advantages for the study of flow instability and evolution (Dimas & Triantafyllou 1994; Shen, Triantafyllou & Yue 2000). However, as it is unsteady, many ensemble runs are needed for the convergence of turbulence statistics. The decaying isotropic turbulence has the advantage of being simple and fundamentally important for theoretical analysis. However, the unsteadiness in the flow and the lack of energy input require a large number of ensemble simulations.

In the present study, we perform direct numerical simulation (DNS) of free-surface turbulence with a new flow configuration, which is statistically steady and homogeneous in the bulk flow below. Isotropic turbulence is generated by the linear forcing method of Lundgren (2003), which supplies turbulence energy in a controllable manner with many of the fundamental properties of isotropic turbulence preserved (Rosales & Meneveau 2005; Guo & Shen 2009). We note that although the Reynolds number in the current DNS does not match the higher values in experiments, the present problem setting has the potential, with the implementation of large-eddy simulation, to correspond directly to experiments of free-surface homogeneous turbulence generated by stirring grids or random jets (e.g. Brumley & Jirka 1987; Herlina & Jirka 2008; Variano & Cowen 2008). The present paper serves as the first step towards the numerical study of maintained isotropic turbulence interacting with a free surface.

Besides the statistically steady and homogeneous turbulence, another feature of the present study is the emphasis on the effect of free-surface deformation with finite amplitude. Fully nonlinear free-surface boundary conditions are used in our simulation, and a systematic investigation on the effect of Froude and Weber numbers is performed. We note that most of the previous numerical and theoretical studies on free-surface turbulence focused on two extreme cases: flat surfaces (e.g. Leighton *et al.* 1991; Handler *et al.* 1993; Pan & Banerjee 1995; Walker *et al.* 1996) and air–water highly mixed flow (e.g. Hong & Walker 2000; Brocchini & Peregrine 2001; Brocchini 2002; Watanabe, Saeki & Hosking 2005). For the situation where the surface has a finite deformation, although effects such as surface vorticity have long been recognized (e.g. Lugt 1987; Longuet-Higgins 1998; Lundgren & Koumoutsakos 1999; Dopazo,

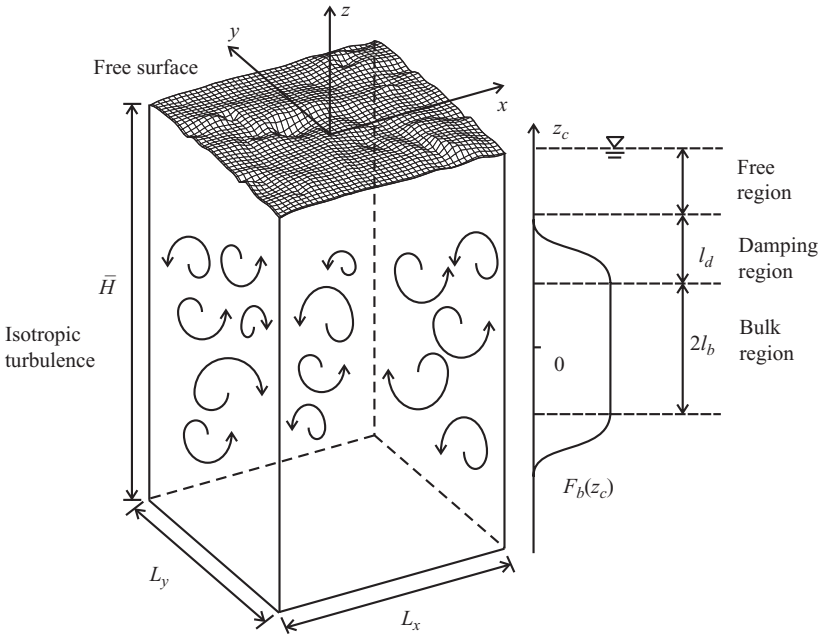

FIGURE 1. Schematics of isotropic turbulence interacting with a deformable free surface.

Lozano & Barreras 2000; Dabiri & Gharib 2001), simulations have been rare. Borue *et al.* (1995) considered small surface deformation and used linearized free-surface boundary conditions to study the one-way effect of turbulence on surface wave motion. Also using linearized surface boundary conditions, Shen *et al.* (1999) showed that the non-zero Froude number affects inter-component energy transfer. Hodges & Street (1999) performed large-eddy simulation, with nonlinear free-surface boundary conditions, for open-channel turbulent flows with and without finite-amplitude surface waves. They found that in the presence of surface waves, the vertical motion of the turbulence near the free surface is enhanced, and the turbulent velocity fluctuations are wave-phase-dependent. They also found that resonant short-crested waves can be generated in the cross-channel direction.

This paper is organized as follows. In § 2, we introduce the problem definition and the numerical method. In § 3, we discuss the surface properties of the flow. In § 4, we study the effect of the free surface on turbulence statistics. In § 5, we study the effect of the characteristic flow structures of splat and antisplat on turbulence anisotropy and the influence of the surface deformation. Finally, we present the conclusions in § 6.

2. Problem definition and numerical method

2.1. *Problem definition*

We consider DNS of a three-dimensional incompressible turbulent water flow below a deformable free surface. As shown in figure 1, isotropic turbulence is generated in the centre region of the computational domain. The turbulence is transported to the near-surface region and interacts with the free surface. We focus on the case where there is no strong wind above the free surface and the air motion is driven by the water flow. As a result, the effect of the air on the free surface is much smaller than

that of the water. For simplification, we set the domain above the free surface to be vacuum, because this approximation causes only small differences from the viewpoint of gravity and surface tension of the interface.

In numerical simulations, isotropic turbulence is usually generated by energy injection at low wavenumbers in the spectral space. For the present problem, however, the inhomogeneity in the vertical direction prevents the use of Fourier transform. To overcome this difficulty, we use the linear forcing method introduced by Lundgren (2003) to generate turbulence, wherein a force proportional to the instantaneous velocity fluctuation is added to the momentum equations in the physical space. To avoid the generation of spurious interfacial phenomena, this force vanishes near the free surface according to

$$\boldsymbol{f} = a_0 F_b\,[z_c]\,\boldsymbol{u}. \tag{2.1}$$

Here $\boldsymbol{u}$ is the instantaneous velocity, which is the same as the turbulent velocity fluctuation because there is no mean flow; a_0 is the force parameter at the centre of the computational domain. The force distribution function $F_b[z_c]$ varies with z_c, the vertical distance to the centre of the computational domain, as (Guo & Shen 2009)

$$F_b[z_c] = \begin{cases} 1 & z_c \leqslant l_b, \quad \text{bulk region,} \\ \dfrac{1}{2}\left(1 - \cos\left[\dfrac{\pi}{l_d}\,(z_c - l_b - l_d)\right]\right) & l_b < z_c \leqslant l_b + l_d, \quad \text{damping region,} \\ 0 & z_c > l_b + l_d, \quad \text{free region,} \end{cases} \tag{2.2}$$

where l_b is half of the vertical length of the bulk region and l_d is the length of the damping region (figure 1).

2.2. *Governing equations and boundary conditions*

In the present study, the frame of reference has axes x, y and z (also denoted as x_1, x_2 and x_3), with x and y horizontal and z vertical. The $+z$ points upwards, with the $z = 0$ plane coinciding with the undisturbed free surface.

The governing equations for the velocity components u_i (also denoted as u, v or w) are the Navier–Stokes equations

$$\frac{\partial u_i}{\partial t} + \frac{\partial (u_i u_j)}{\partial x_j} = -\frac{\partial p}{\partial x_i} + \frac{1}{Re}\frac{\partial^2 u_i}{\partial x_j \partial x_j} + a_0 F_b\,[z_c]\,u_i, \quad i = 1, 2, 3, \tag{2.3}$$

and the continuity equation

$$\frac{\partial u_i}{\partial x_i} = 0. \tag{2.4}$$

Here and hereafter, unless otherwise indicated, all variables are normalized by a characteristic length scale L and a characteristic velocity scale U, the choice of which is discussed in § 2.4. The dynamic pressure p is normalized by ρU^2, where ρ is the density. The Reynolds number is defined as $Re = UL/\nu$, with ν the kinematic viscosity.

At the free surface, the KBC is

$$\frac{\partial \eta}{\partial t} + u\frac{\partial \eta}{\partial x} + v\frac{\partial \eta}{\partial y} - w = 0 \qquad \text{at} \quad z = \eta. \tag{2.5}$$

Here η is the elevation of the free surface. The DBCs are given as follows.

(*a*) At the free surface, the tangential stresses vanish:

$$\boldsymbol{t}_1 \cdot [\boldsymbol{\Gamma}] \cdot \boldsymbol{n}^T = 0, \qquad \boldsymbol{t}_2 \cdot [\boldsymbol{\Gamma}] \cdot \boldsymbol{n}^T = 0. \tag{2.6}$$

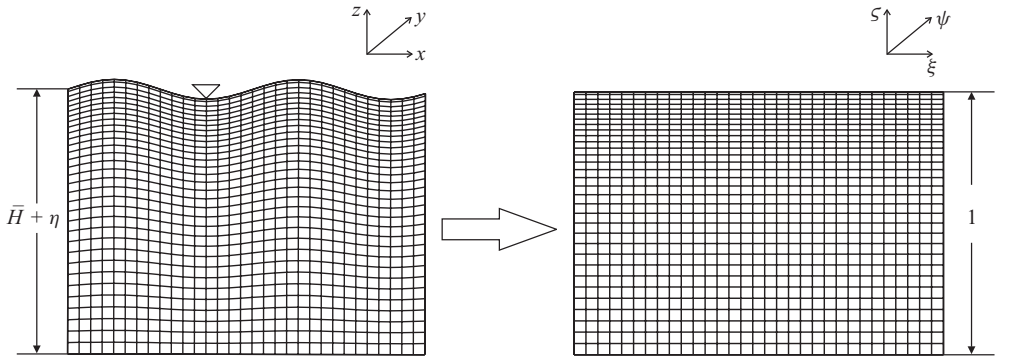

FIGURE 2. Sketch plot of the algebraic mapping that transforms the irregular Cartesian space (x, y, z, t) confined by the free surface to a rectangular computational domain $(\xi, \psi, \varsigma, \tau)$.

In the above equation, $[\boldsymbol{\Gamma}]$ is the stress tensor expressed as $\boldsymbol{\Gamma}_{ij} = -P\delta_{ij} + (u_{i,j} + u_{j,i})/Re$. Here δ_{ij} is the Kronecker delta and $P = p - z/Fr^2$, where the Froude number is defined as $Fr = U/\sqrt{gL}$, with g the gravitational acceleration. And $\boldsymbol{n}$ is the unit vector normal to the free surface pointing to the vacuum side; $\boldsymbol{t}_1$ and $\boldsymbol{t}_2$ are unit vectors tangential to the free surface. They are expressed as

$$\boldsymbol{n} = \frac{(-\eta_x, -\eta_y, 1)}{\sqrt{\eta_x^2 + \eta_y^2 + 1}}, \qquad \boldsymbol{t}_1 = \frac{(1, 0, \eta_x)}{\sqrt{\eta_x^2 + 1}}, \qquad \boldsymbol{t}_2 = \frac{(0, 1, \eta_y)}{\sqrt{\eta_y^2 + 1}}. \tag{2.7}$$

In (2.6), $\boldsymbol{n}^T$ denotes the transpose of $\boldsymbol{n}$.

(*b*) At the free surface, the force balance in the surface-normal direction gives

$$\boldsymbol{n} \cdot [\boldsymbol{\Gamma}] \cdot \boldsymbol{n}^T = \frac{1}{We}\left(\frac{1}{R_1} + \frac{1}{R_2}\right), \tag{2.8}$$

where $We = \rho U^2 L/\gamma$ is the Weber number, with γ the surface tension coefficient; and $1/R_1$ and $1/R_2$ are the principal curvatures of the surface that satisfy

$$\frac{1}{R_1} + \frac{1}{R_2} = \frac{\left(1 + \eta_x^2\right)\eta_{yy} + \left(1 + \eta_y^2\right)\eta_{xx} - 2\eta_x\eta_y\eta_{xy}}{\left(1 + \eta_x^2 + \eta_y^2\right)^{3/2}}. \tag{2.9}$$

At the bottom $z = -\overline{H}$, a free-slip boundary condition is imposed as $\partial u/\partial z = \partial v/\partial z = 0$ and $w = 0$. In the horizontal directions, the periodic boundary condition is applied.

2.3. *Numerical scheme*

In the simulation of free-surface turbulence, a major issue is that the surface geometry is irregular and it changes with time. In the present study, we employ a boundary-fitted grid. The irregular space (x, y, z, t) confined by the free surface is transformed to a rectangular computational domain $(\xi, \psi, \varsigma, \tau)$ using an algebraic mapping (Guo & Shen 2009):

$$\tau = t, \qquad \xi = x, \qquad \psi = y, \qquad \varsigma = \frac{z + \overline{H}}{\eta + \overline{H}}. \tag{2.10}$$

A sketch plot of the mapping is shown in figure 2. With this transform, the vertical dimension is normalized by $\eta + \overline{H}$, while the horizontal dimensions are kept the same.

From the physical space to the computational space, the vertical grid lines remain vertical and the grid points along these lines are stretched.

Using the chain rule, we have

$$\left.\begin{aligned}\frac{\partial}{\partial t} &= \frac{\partial}{\partial \tau} - \frac{\varsigma \eta_t}{\eta + \overline{H}} \frac{\partial}{\partial \varsigma},\\ \frac{\partial}{\partial x} &= \frac{\partial}{\partial \xi} - \frac{\varsigma \eta_x}{\eta + \overline{H}} \frac{\partial}{\partial \varsigma},\\ \frac{\partial}{\partial y} &= \frac{\partial}{\partial \psi} - \frac{\varsigma \eta_y}{\eta + \overline{H}} \frac{\partial}{\partial \varsigma},\\ \frac{\partial}{\partial z} &= \frac{1}{\eta + \overline{H}} \frac{\partial}{\partial \varsigma}.\end{aligned}\right\} \tag{2.11}$$

The governing equations and the boundary conditions are then rewritten in terms of $(\xi, \psi, \varsigma, \tau)$ (Guo & Shen 2009). The numerical scheme we use is based on the fractional-step method discussed in Kim & Moin (1985). We use a second-order Crank–Nicholson scheme for the viscous terms and a second-order Adams–Bashforth scheme for the convective terms. The surface elevation is advanced in time with a second-order Runge–Kutta scheme. For space discretization, in the ξ and ψ directions, we use a pseudospectral method with Fourier series; in the ς direction, we use a second-order finite-difference scheme on a staggered grid (Harlow & Welch 1965). Numerical details of our DNS and its validation are provided in Guo & Shen (2009) and Guo (2010).

We note that the algebraic mapping (2.10) is not conformal. As pointed out by Hodges & Street (1999), who used an orthogonal and boundary-fitted grid to simulate dynamically evolving free-surface flows, conformal mapping is accurate and expensive, and is unnecessary for problems with small surface elevations. In addition, Nielsen & Skovgaard (1990) and Sankaranarayanan & Spaulding (2003) showed that the error caused by the non-orthogonality of the grid is acceptable when the grid distortion angle is less than 40°. The angle is one order of magnitude smaller in the current problem. Therefore, for the present study, we choose the algebraic mapping for simplicity.

2.4. *Computational parameters*

In the present study, the dimensionless computational domain size is $L_x \times L_y \times \overline{H} = 2\pi \times 2\pi \times 5\pi$. In other words, the characteristic length scale L is set to be $1/(2\pi)$ of the horizontal domain size. The vertical lengths of the bulk region, the damping region and the free region are 3π, $\pi/2$ and $\pi/2$, respectively. As shown by Guo & Shen (2009), for the linear forcing magnitude variation given by (2.2), this choice of region lengths produces a $(2\pi)^3$ cubic of isotropic turbulence at the centre of the computational domain, which serves as a reservoir for homogeneous turbulence supply. In their isotropic and homogeneous simulation cases, Rosales & Meneveau (2005) showed that the integral length scale of turbulence, L_∞, is 19 % of the domain size for the range of $Re_\lambda = u^{rms}\lambda/\nu \in (30, 153)$ tested (our Re_λ is within this range). Here Re_λ is the Taylor-scale Reynolds number; the superscript 'rms' denotes the root-mean-square value; and λ is the Taylor scale.

The characteristic velocity scale U is not set *ad hoc* (Rosales & Meneveau 2005). Instead, it is determined by the characteristic length scale chosen and the value of a_0 (set to be 0.1 in the present study; note that $1/a_0$ is a time scale as shown in (2.3)). Based on the theory of isotropic turbulence, in the bulk flow, if balance between the

dissipation rate and the rate of energy injection by the linear force is assumed, it can be shown that $u^{rms} = 3a_0 L_\infty$ (which is confirmed by the numerical data; for details see Guo & Shen 2009). Finally, we set Re in (2.3) to be 1000 in our DNS.

The above analysis is for the isotropic turbulence in the bulk flow. Towards the free surface, the magnitude of the linear forcing diminishes according to (2.2) and the turbulence level decays over the damping region and the free region. At the centre of the free region ($z = -\pi/4$), we found $u^{rms} = 0.090$, $\lambda = 0.339$ and $Re_\lambda = 30.39$ (details are given in Guo & Shen 2009 with empirical parametrizations provided in (38) there). We remark that as will be shown in the subsequent sections, the flow at $z = -\pi/4$ is considered to be representative of the isotropic turbulence before it interacts with the free surface. For the isotropic turbulence at $z = -\pi/4$, we can obtain the integral scale as $L_\infty = \lambda Re_\lambda/15 = 0.69$ (Tennekes & Lumley 1972).

In previous experiments of stirring-grid turbulence under a free surface, it is conventional to quantify a turbulent Reynolds number defined as $Re_L = u^{rms}(2L_\infty)/\nu$ (following Tennekes & Lumley 1972). The value of Re_L is 365.7 in Brumley & Jirka (1987) (for the case they studied in detail), and ranges from 282 to 974 in McKenna & McGillis (2004) and from 260 to 780 in Herlina & Jirka (2008). In our simulation, Re_L at the centre of the free region is only 123.2 because of the limitation of DNS to low Reynolds numbers. The large difference in the Reynolds number makes the direct comparison between our DNS and measurements in the literature difficult. Nevertheless, in the following sections, we will make qualitative comparison when possible.

In the present study, we use a $128 \times 128 \times 348$ grid. The total grid number is relatively small compared with that of modern simulations with rectangular domain (e.g. Sullivan & Patton 2008), because of the substantial increase in the computational cost caused by the boundary-fitted grid. Our grid is evenly distributed in the horizontal directions, with the grid size $\Delta_x = \Delta_y = 2\pi/128 = 0.049$. In the vertical direction, the grid is clustered towards the free surface. The maximum grid size is $\Delta_{z,max} = \Delta_x = 0.049$ below the free region, and the minimum is $\Delta_{z,min} = 0.0025$ at the free surface. The thickness of the free-surface viscous layer is estimated as $L_\nu = L_\infty/Re_L^{1/2} = 0.062$ (Brumley & Jirka 1987). Hodges & Street (1999) pointed out that 5 grid points are needed within the viscous layer, and they used 10 points in their simulation. In the current study, 12 points exist inside the viscous layer. As will be shown in the subsequent sections, the surface layer structure is resolved adequately.

On the basis of the theory of isotropic homogeneous turbulence (Tennekes & Lumley 1972), we estimate the Kolmogorov scale at the centre of the free region as $\eta_K \sim \lambda/(15^{1/4} Re_\lambda^{1/2}) \approx 0.031$, which is comparable to Δ_x. To ensure that all the dynamically important structures of the turbulence are resolved, we have tested with a finer $256 \times 256 \times 575$ grid and a coarser $64 \times 64 \times 170$ grid. Figure 3(a, b) shows that the difference of the result of the current $128 \times 128 \times 348$ grid from the coarser grid result is noticeable, while that from the finer grid result is negligibly small. Therefore, the current resolution is necessary and adequate to obtain grid-independent results.

The values of Fr and We, which govern the surface deformation, are listed in table 1 for the simulation cases in the present study. We note that the fluctuation of the surface elevation, η^{rms}, is relatively small. The presence of the water and the vacuum is intermittent in a thin region near $z = 0$, which we define as the surface intermittency layer (in addition to the aforementioned surface source layer and surface viscous layer). For the cases considered in our study, we found that the volume fraction of the water is larger than 98 % below $z = -2\eta^{rms}$, which we define as the lower boundary of the intermittency layer. From the η^{rms} value listed in table 1, we see that the intermittency layer is very thin in the present study.

Case	Fr^2	We	k_{cr}	η^{rms}	$E_p/(2\eta^{rms}\widetilde{E}_{k,\tilde{d}=0})$	$E_p/(2\eta^{rms}\widetilde{E}_{k,\tilde{d}=-\pi/4})$
A1	0.1	40	20	0.00337	0.374	0.520
B0	0.2	∞	∞	0.00722	0.383	0.386
B1	0.2	40	14.14	0.00658	0.343	0.359
B2	0.2	20	10	0.00626	0.321	0.348
C1	0.8	40	7.07	0.0158	0.234	0.231

TABLE 1. Free surface parameters considered in the present study.

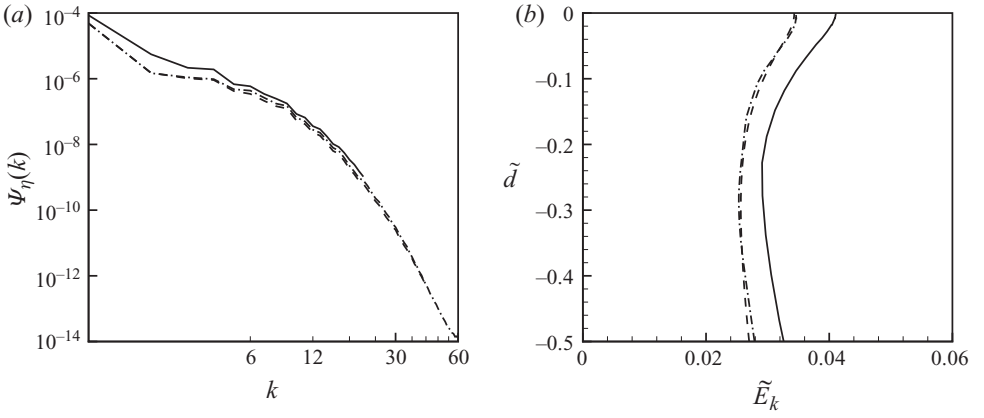

FIGURE 3. Comparison of (*a*) surface elevation spectrum, and (*b*) vertical profile of turbulent kinetic energy for case B1 among different DNS resolutions: ——, a $64 \times 64 \times 170$ grid; – – –, a $128 \times 128 \times 348$ grid; – · – · –, a $256 \times 256 \times 575$ grid. The details for the quantification of the surface elevation spectrum and the turbulent kinetic energy are discussed in §§ 3.1 and 4.1, respectively.

To illustrate flat-surface results, we use the case of A1, of which the surface elevation is the smallest among the cases listed in table 1. It should be pointed out that ideally, simulation with an exactly flat surface should be used, which requires another code with different free-surface boundary condition formulation and numerical scheme. To eliminate the difference caused by the numerical methods, we decide to stay with the same code using a sufficiently small Fr to ensure the comparison is faithful. We also remark that Fr as small as possible would be preferred; however, we found that the term z/Fr^2 in the DBC may amplify the numerical errors associated with η and thus deteriorate the results. As will be shown in § 4.1, the case of A1 is an acceptable proxy because the result of turbulence statistics is close to the previous flat-surface results, whereas for other cases listed in table 1 the effect of surface deformation is noticeable.

In the present study, we first run the simulation for 17 large-eddy turnover times (based on the quantities in the bulk flow) to ensure the turbulence is fully developed under the linear forcing and is independent of the initial flow field (Rosales & Meneveau 2005). We then continue the simulation for another 48 turnover times, which is equivalent to about 20 large-eddy turnover times based on the quantities in the free region. Because the flow is statistically steady, turbulence statistics can be obtained with samples taken at different times. In other words, it is not required to have ensemble runs like the previous free-surface simulations of unsteady sheared turbulence or decaying homogeneous turbulence reviewed in § 1.

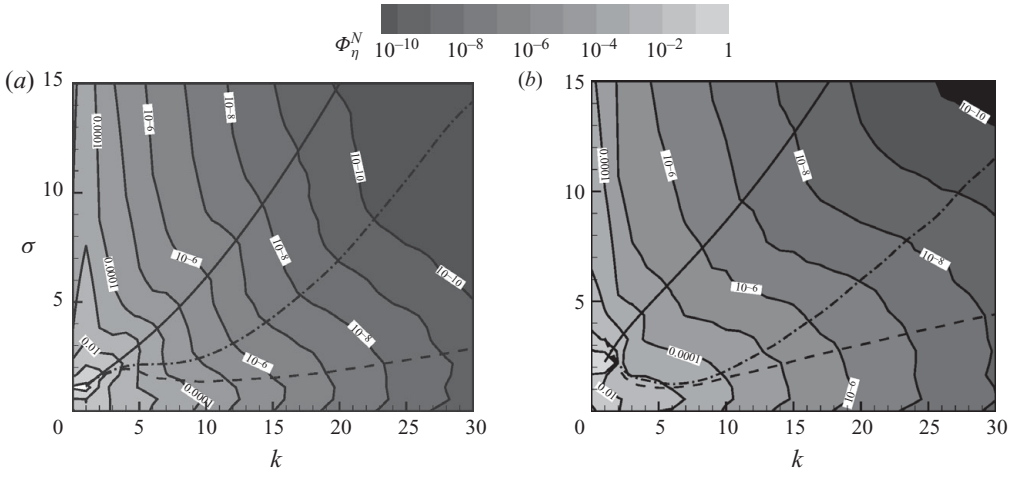

FIGURE 4. Normalized frequency–wavenumber spectrum of the surface elevation for the cases of (*a*) C1 and (*b*) B1: ——, dispersion relationship (3.2); – – –, characteristic frequency based on the fully nonlinear KBC (3.3); – · – · –, characteristic frequency based on the linearized KBC (3.4).

3. Surface deformation and waves

3.1. *Surface waves and turbulence-induced roughness*

In free-surface turbulence, the deformable surface is disturbed by the turbulence underneath. The free surface can respond passively, in the form of surface roughness, to the local pressure fluctuation in the turbulent flow. It can also have a large elevation caused by the impingement of coherent turbulence structures such as splats on the surface; the large surface deformation then propagates away in the form of surface waves. Tryggvason (1988) showed that short waves can be generated by a vortex sheet below a free surface. Borue *et al.* (1995) studied the characteristic frequency of turbulence and the frequency spectrum of surface elevation in an open-channel flow. Teixeira & Belcher (2006) used the rapid distortion theory to study the wave generation caused by the turbulence in air and water, and found the latter dominant in the wave generation process. Savelsberg & van de Water (2009) quantified in detail gravity–capillary waves in a channel with turbulence excited by an active grid.

For the current case in which the surface is excited by the homogeneous turbulence from below, we have observed surface roughness in the form of dimples (associated with surface-connected vortices) as well as scars (associated with near-surface horizontal vortices), consistent with the review by Sarpkaya (1996). We have also observed propagating surface waves generated by the large disturbance of coherent turbulence structures, mainly splats impinging on the free surface (not shown here due to space limitation; the direct observation is also supported by the statistical result of the spatial–temporal correlation of surface divergence and surface elevation).

Next, we examine these two types of surface deformation through the frequency–wavenumber spectrum of the surface elevation

$$\Phi_\eta^N(|\boldsymbol{k}|,\sigma)=\frac{1}{(2\pi)^3\cdot(\eta^{rms})^2}\int_T\int_S\overline{\eta(\boldsymbol{x},t)\,\eta(\boldsymbol{x}+\boldsymbol{r},t+\tau)}\cdot\mathrm{e}^{-\mathrm{i}(\boldsymbol{k}\cdot\boldsymbol{r}+\sigma\tau)}\,\mathrm{d}\boldsymbol{r}\,\mathrm{d}\tau. \tag{3.1}$$

Here T is the sampling duration, S denotes the horizontal plane and the overline ($\bar{}$) denotes averaging. Figure 4 shows Φ_η^N for the representative cases of C1 and B1. For

case C1, which has the largest surface deformation, energy is concentrated on two ridges in the contour plot, one with relatively high frequency and the other with low frequency. For the case of B1, the two ridges still exist, with the high-frequency one manifesting in the region of small values of wavenumber k and frequency σ.

It is found that the two ridges correspond to propagating surface waves and turbulence-induced surface roughness, respectively. To show the waves, we consider the dispersion relationship for small-amplitude deep-water waves:

$$\sigma = \sqrt{\frac{k}{Fr^2} + \frac{k^3}{We}}, \tag{3.2}$$

which is plotted in figure 4 as solid lines. The dispersion relationship coincides with the high-frequency ridge at low k, signifying the existence of surface waves at large scales. We remark that because of the use of the periodic boundary condition in our simulation, standing waves may be formed (Dommermuth 1994; Guo & Shen 2009). We examined the energy of propagating and standing waves, and found the latter is one to two orders of magnitude smaller than the former. Therefore, the evidence of large-scale waves obtained from the frequency–wavenumber spectrum is not a numerical artifact.

In figure 4, the dispersion relationship does not manifest in the spectrum contours when k is large. This is not surprising, because short waves are quickly damped due to viscous dissipation, which are effective at large k.

To investigate the surface roughness associated with the turbulence motion, we quantify a characteristic frequency of η at each k as

$$\sigma = \sqrt{\frac{\Psi_\eta(k)}{\Psi_{\eta_t}(k)}}. \tag{3.3}$$

We also consider the expression used by Borue *et al.* (1995):

$$\sigma = \sqrt{\frac{\Psi_\eta(k)}{\Psi_w(k)}}. \tag{3.4}$$

In both (3.3) and (3.4), a one-dimensional spatial spectrum is defined as

$$\Psi_q(|\boldsymbol{k}|) = \frac{1}{(2\pi)^2} \int_S \overline{q(\boldsymbol{x}, t)\, q(\boldsymbol{x} + \boldsymbol{r}, t)} \cdot \mathrm{e}^{-\mathrm{i}\boldsymbol{k}\cdot\boldsymbol{r}}\, \mathrm{d}\boldsymbol{r}. \tag{3.5}$$

The difference between (3.3) and (3.4) is that the former takes into account the nonlinearity of the surface motion ($\eta_t = w - u\eta_x - v\eta_y$), while the latter is a linearized approximation ($\eta_t \approx w$).

Figure 4 shows that (3.3) corresponds to the low-frequency ridge. We note that the agreement is approximate and is in the average sense. For example, at low k, for all the cases including the ones not shown in figure 4 because of space limitation, the ridge exists at a frequency slightly lower than the prediction by (3.3); at high k, the ridges in the cases of B2 (not shown) and C1 have higher and lower σ, respectively. In general, the nonlinear expression (3.3) works better than the linearized one (3.4). The difference between (3.3) and (3.4) becomes larger as k increases, indicating the nonlinear effect at large k. We note that the importance of surface nonlinearity was recently shown by Savelsberg & van de Water (2009) using their measurement.

In summary, the frequency–wavenumber spectrum of surface elevation shows that the surface deformation can be related to the dispersion relationship for surface waves

and the nonlinear-KBC-based characteristic frequency for turbulence-induced surface roughness. The waves exist mainly at small k. The turbulence-induced roughness occurs over a wide range of k because of the turbulent motions at the corresponding scales. As shown in figure 4, at small k, the frequencies between the two types of surface deformation is close to each other, indicating that waves may be excited by turbulence structures at large scales. At large k, the gap between the two frequencies becomes large. As a result, turbulence-induced roughness dominates at large k, and small-scale waves are dissipated by the turbulence underneath rather than excited by it (see e.g. Kitaigorodskii & Lumley 1983; Olmez & Milgram 1992; Teixeira & Belcher 2002; for the detailed process of wave–turbulence interaction, which is beyond the scope of the present paper, more analysis is needed and will be performed in our future study).

3.2. *Spatial statistics of surface deformation and dependence on Fr and We*

The surface deformation depends on gravity and surface tension, of which the effects are related to *Fr* and *We*, respectively. Their relative importance is associated with a critical wavenumber (Phillips 1958):

$$k_{cr} = \sqrt{\frac{We}{Fr^2}}. \tag{3.6}$$

The values of k_{cr} of the simulation cases in the present study are listed in table 1. The physical meaning of k_{cr} can be understood by considering a sinusoidal surface deformation with wavenumber k and amplitude a_k. The (dimensionless) density of gravitational potential energy is

$$\widehat{E}_g(k) = \frac{1}{2Fr^2} \cdot \frac{1}{S} \int_S \eta^2 \, \mathrm{d}x \, \mathrm{d}y = \frac{a_k^2}{4Fr^2}. \tag{3.7}$$

For small a_k, the density of surface tension potential energy is

$$\begin{aligned} \widehat{E}_\gamma(k) &= \frac{1}{We} \int_S \left[\sqrt{1 + \left(\frac{\partial \eta}{\partial x}\right)^2 + \left(\frac{\partial \eta}{\partial y}\right)^2} - 1 \right] \mathrm{d}x \, \mathrm{d}y \\ &\approx \frac{1}{We} \cdot \frac{1}{2S} \int_S \left[\left(\frac{\partial \eta}{\partial x}\right)^2 + \left(\frac{\partial \eta}{\partial y}\right)^2 \right] \mathrm{d}x \, \mathrm{d}y = \frac{k^2 a_k^2}{4We}. \end{aligned} \tag{3.8}$$

Therefore, the ratio between the two types of potential energy is

$$\frac{\widehat{E}_\gamma(k)}{\widehat{E}_g(k)} \approx \frac{Fr^2}{We} k^2 = \left(\frac{k}{k_{cr}}\right)^2. \tag{3.9}$$

When $k < k_{cr}$, $\widehat{E}_g(k)$ is larger than $\widehat{E}_\gamma(k)$; whereas when $k > k_{cr}$, $\widehat{E}_\gamma(k)$ is larger.

In this study, we examine $\widehat{E}_g(k)$ and $\widehat{E}_\gamma(k)$ as functions of k using the simulation data of η. For the results to be more insightful, we decompose η into a wave component (denoted by the subscript '*wave*') and a turbulence roughness component (denoted by the subscript '*turb*'). The decomposition is performed on the basis of the frequency–wavenumber spectrum discussed in § 3.1, with the boundary between the wave and turbulence regions defined as the fastest descending line in the valley separating the two ridges. The obtained $\widehat{E}_{g,wave}(k)$ and $\widehat{E}_{g,turb}(k)$ are plotted in figure 5 for the cases of A1, B1, B2 and C1 (case B0 does not have surface tension). Note that

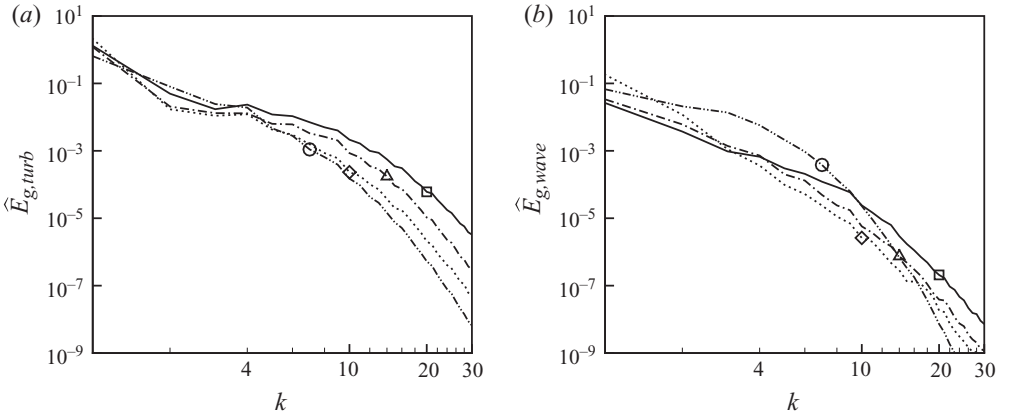

FIGURE 5. (*a*) $\widehat{E}_{g,turb}(k)$ and (*b*) $\widehat{E}_{g,wave}(k)$, both normalized by $(2\eta^{rms}\widetilde{E}_{k,\widetilde{d}=0})$: ——, case A1; – · – · –, case B1; · · · · · ·, case B2; – · · – · · –, case C1. The critical wavenumber k_{cr} is marked as: □, case A1; △, case B1; ◇, case B2; ○, case C1.

$\widehat{E}_{\gamma,wave}(k)$ and $\widehat{E}_{\gamma,turb}(k)$ can be obtained, respectively, from $\widehat{E}_{g,wave}(k)$ and $\widehat{E}_{g,turb}(k)$ on the basis of (3.9).

In figure 5, the location of k_{cr} is marked by a symbol for each case. The potential energy density is normalized by $(2\eta^{rms}\widetilde{E}_{k,\widetilde{d}=0})$. Here $\widetilde{E}_{k,\widetilde{d}=0} = [(\widetilde{u}^{rms}_{\widetilde{d}=0})^2 + (\widetilde{v}^{rms}_{\widetilde{d}=0})^2 + (\widetilde{w}^{rms}_{\widetilde{d}=0})^2]/2$ is the density of the kinetic energy at the free surface; $\widetilde{d}$ denotes the signed distance to the free surface, with the minus sign corresponding to the waterside (see Appendix A). The quantity $(2\eta^{rms}\widetilde{E}_{k,\widetilde{d}=0})$ gives a measure of the kinetic energy contained in the intermittency layer (of which the thickness can be quantified as $2\eta^{rms}$; see § 2.4). Let E_p denote the density of the total potential energy

$$E_p = \int \left[\widehat{E}_{g,wave}(k) + \widehat{E}_{g,turb}(k) + \widehat{E}_{\gamma,wave}(k) + \widehat{E}_{\gamma,turb}(k)\right] \mathrm{d}k. \tag{3.10}$$

Table 1 shows that E_p is about 23.4–38.3 % of $(2\eta^{rms}\widetilde{E}_{k,\widetilde{d}=0})$ for the cases considered in the present study. For reference, we also show in table 1 the normalization using $(2\eta^{rms}\widetilde{E}_{k,\widetilde{d}=-\pi/4})$, that is, on the basis of the interior kinetic energy (cf. § 4). The difference between these two methods of normalization is caused by the vertical variation of the kinetic energy near the free surface, which is affected by the surface deformation (discussed in § 4).

First, we compare the gravitational potential energy and the surface tension potential energy for both the wave and turbulence components. Equation (3.9) indicates that $\widehat{E}_g(k)$ dominates $\widehat{E}_\gamma(k)$ when $k < k_{cr}$. Because the linearly forced turbulence has the largest energy at the smallest wavenumber (Rosales & Meneveau 2005), the excited surface deformation decreases monotonically as k increases. As a result, more potential energy is associated with the gravity than that with the surface tension. In a way similar to (3.10), we define the total potential energy for each component, namely $E_{g,wave}$, $E_{g,turb}$, $E_{\gamma,wave}$ and $E_{\gamma,turb}$; their ratios to E_p are listed in table 2. It shows that the weight of the total surface tension potential energy $E_\gamma = E_{\gamma,wave} + E_{\gamma,turb}$ in E_p increases as k_{cr} decreases, with the minimum $E_\gamma/E_p \approx 1.4\,\%$ for case A1 and the maximum $E_\gamma/E_p \approx 8.4\,\%$ for case C1.

Case	$E_{g,wave}/E_p$	$E_{g,turb}/E_p$	$E_{\gamma,wave}/E_p$	$E_{\gamma,turb}/E_p$
A1	0.0217	0.964	0.000290	0.0143
B1	0.0316	0.951	0.000615	0.0169
B2	0.0293	0.930	0.00319	0.0376
C1	0.102	0.813	0.0191	0.0652

TABLE 2. The ratios of gravitational and surface tension energy associated with wave and turbulence motions to the total potential energy.

The surface tension potential energy dominates the gravitational potential energy for $k > k_{cr}$ only. Although the total potential energy associated with the surface tension is relatively low as discussed above, it can change the appearance of the free surface substantially. From cases B0 to B1 to B2, Fr^2 is fixed at 0.2 while We changes from ∞ to 40 to 20; we found that the instantaneous surface becomes much smoother (not plotted), and the kurtosis of the surface elevation reduces from 3.29 to 3.19 to 2.33.

Equations (3.7)–(3.8) show that the gravitational potential energy scales with the square of the surface elevation divided by Fr^2, while the surface tension potential energy scales with the square of the surface slope divided by We. Between two flows, if they have the (Fr, We) combinations such that the resultant values of k_{cr} are identical, the partition between $\widehat{E}_g(k)$ and $\widehat{E}_\gamma(k)$ would be the same. If we have the additional conditions that the excitations of the underlying turbulence on the free surface are the same (i.e. $\widehat{E}_p(k)/(2\eta^{rms}\widetilde{E}_{k,\tilde{d}=-\pi/4})$ is identical) and that the difference caused by the energy redistribution among different wave modes is negligible, the surface fluctuation would scale with Fr^2 and We. While the k_{cr} value may be adjusted with (Fr, We) changed, the above-mentioned additional conditions may not be easy to satisfy. In this study, we did not find a simple scaling law for the surface fluctuation that is applicable to the general situations.

Next, we compare the potential energy associated with the waves to that associated with the turbulence-induced surface roughness. For the cases of A1, B1 and B2, figure 5 shows that the former is much lower than the latter, especially at high wavenumbers. Therefore, although energy of the order of $(2\eta^{rms}\widetilde{E}_{k,\tilde{d}=0})$ can be transferred to the potential energy, only a small portion is turned into waves. Table 2 shows that the weights of $E_{wave} = E_{g,wave} + E_{\gamma,wave}$ in E_p are 2.2 %, 3.2 % and 3.2 % for cases A1, B1 and B2, respectively. In the case of C1, on the other hand, the waves become much more pronounced, with E_{wave}/E_p increasing to 12.1 %. For low to intermediate k, $\widehat{E}_{g,wave}(k)$ and $\widehat{E}_{\gamma,wave}(k)$ of case C1 are much elevated compared with other cases (figure 5). This result is consistent with the previously discussed figure 4, which shows that case C1 has a distinct wave ridge in the frequency–wavenumber spectrum.

We note that for the dominant wave components, the wave phase speed c_p is about one order of magnitude larger than the turbulent velocity fluctuation $\widetilde{u}^{rms}_{\tilde{d}=0}$ (details about its quantification are given in § 4). Table 3 lists the values of $c_p/\widetilde{u}^{rms}_{\tilde{d}=0}$ for the first five wave modes. On the other hand, because of the small wave amplitude, the orbital velocity of the waves is about two orders of magnitude smaller than the turbulence fluctuation (also shown in table 3). Not surprising, the distortion effect of the waves on the turbulence (Teixeira & Belcher 2002) is thus negligibly small in the current problem.

	$c_p/\widetilde{u}^{rms}_{\widetilde{d}=0}$					$u_{orb}(k)/\widetilde{u}^{rms}_{\widetilde{d}=0}$				
Case	$k=1$	$k=2$	$k=3$	$k=4$	$k=5$	$k=1$	$k=2$	$k=3$	$k=4$	$k=5$
A1	17.6	12.5	10.3	8.96	8.10	0.0159	0.00851	0.00533	0.00517	0.00393
B1	14.4	10.2	8.47	7.45	6.80	0.0212	0.0128	0.00763	0.00644	0.00388
B2	14.1	10.1	8.48	7.58	7.04	0.0481	0.0176	0.00680	0.00462	0.00278
C1	7.46	5.43	4.64	4.25	4.05	0.0470	0.0381	0.0395	0.0313	0.0226

TABLE 3. The ratios of wave phase velocity and orbital velocity to the horizontal velocity fluctuation at the surface, for wave modes $k=1$–5.

4. Turbulence statistics

In this section, we discuss the effect of the free surface on the statistics of the turbulent flow underneath. It is helpful to summarize here the thickness of the various surface layers quantified in § 2.4. The source layer thickness is quantified by the integral length scale of the underlying turbulence (at $z=-\pi/4$) (Hunt & Graham 1978), which is approximately 0.69 in the current problem. For the viscous layer, its thickness is approximately 0.062. The intermittency layer has the thickness of $2\eta^{rms}$, which is small in the present study (ranging from 0.0067 to 0.032 for the cases listed in table 1).

The DNS data are obtained on the surface-following computational grid of the algebraic mapping discussed in § 2. While such a grid is computationally convenient, the discrete data need to be transformed to other coordinates for a better interpretation of the flow physics. In the present study we use two approaches for flow statistics.

The first approach expresses the statistics as functions of the distance from the free surface, and projects the flow quantities into the local surface-normal and surface-tangential directions. The details of the data transform are provided in Appendix A. This approach is complex, but it has the advantage of being able to capture the vicinity of the free surface and to express the results in terms of the directions normal and tangential to the local surface. We use it in §§ 4.1 and 4.2 for relatively simple turbulence statistics.

The analysis of the kinetic energy budget in § 4.3 is more complex, and a fixed Cartesian coordinate system has to be used. To avoid the complexity associated with the intermittence of the fluid phase at the free surface, we perform analysis for the region below $z=-2\eta^{rms}$ only. In this second approach, linear interpolation in the vertical direction is used when the DNS data are transformed from the computational grid to the Cartesian grid.

4.1. *Velocity fluctuations and turbulent kinetic energy*

We first examine the profiles of the fluctuations of horizontal and vertical velocity components and turbulent kinetic energy shown in figure 6. Here and hereafter, the tilde denotes the projection into the local surface-normal and surface-tangential directions (Appendix A). We normalize the results by the values at the centre of the free region $\widetilde{d}=-\pi/4$, which is just outside the source layer. The turbulence there is nearly isotropic, and we use it as a reference to investigate the anisotropy of the near-surface flow.

From figure 6(*b*), we see that the vertical velocity fluctuation decreases towards the surface over the region $\widetilde{d}>-0.5$, because the surface restrains the vertical motion of

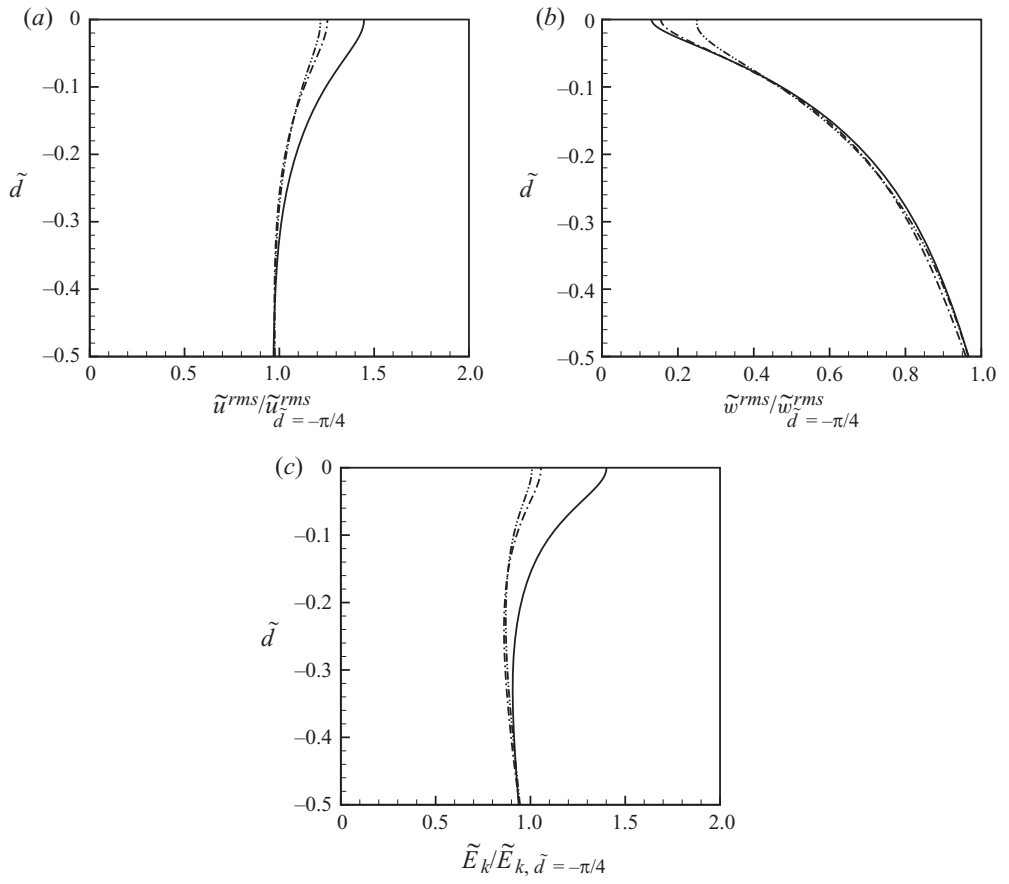

FIGURE 6. Vertical profiles of normalized (*a*) surface-tangential velocity fluctuation, (*b*) surface-normal velocity fluctuation and (*c*) turbulent kinetic energy $\widetilde{E}_k$ near the free surface: ——, case A1; – · – · – , case B1; – · · – · · – , case C1.

the fluid. For the horizontal velocity fluctuation (figure 6*a*), it increases towards the surface. This increase has been observed in experiments (see e.g. Brumley & Jirka 1987; McKenna & McGillis 2004; Variano & Cowen 2008) and simulations (see e.g. Walker *et al.* 1996). Over the region $\widetilde{d} > -0.5$, the horizontal velocity increases by about 45 %, which is consistent with the results of Brumley & Jirka (1987) and Walker *et al.* (1996) and is larger than the 22 % increase predicted by the inviscid rapid distortion theory of Hunt & Graham (1978). Near the surface, in addition to the energy redistribution from the vertical to horizontal velocity components, the change in viscous dissipation also contributes to the variation in velocity fluctuations. The dynamic free-surface boundary condition of vanishing surface-tangential stresses results in significant reduction of the viscous dissipation (Teixeira & Belcher 2000). As a result, the kinetic energy accumulates near the free surface (figure 6*c*), which leads to a larger increase of horizontal velocities towards the surface than the prediction of Hunt & Graham (1978).

We note that the case of A1 has an appreciable increase in the kinetic energy towards the free surface. This increase resembles the result of a flat free surface of Walker *et al.* (1996), and is different from other cases with relatively larger surface

deformation. In our investigation of the influence of the surface deformation on the statistics of the near-surface turbulence, we found that among the cases listed in table 1, *Fr* has a relatively larger effect than *We* does. For simplicity, here we focus on the comparison among cases A1, B1 and C1. As *Fr* increases, the blockage effect of the surface decreases. At the free surface, the horizontal velocity fluctuation decreases, and the vertical velocity fluctuation increases. The increase of kinetic energy towards the free surface becomes less significant as the surface becomes more flexible. This phenomenon will be revisited in §§ 4.2 and 5.

4.2. *Fluctuations of velocity gradients*

Next, we study the fluctuations of velocity gradients. On the basis of the horizontal isotropy of the current problem, there are five independent velocity gradients as far as statistics are concerned: $\partial\widetilde{u}/\partial\widetilde{x}$, $\partial\widetilde{u}/\partial\widetilde{y}$, $\partial\widetilde{u}/\partial\widetilde{z}$, $\partial\widetilde{w}/\partial\widetilde{x}$ and $\partial\widetilde{w}/\partial\widetilde{z}$.

Figure 7(*a*, *b*) shows the profiles of $\partial\widetilde{u}/\partial\widetilde{x}$ and $\partial\widetilde{w}/\partial\widetilde{z}$ fluctuations. They increase as the free surface is approached, signifying the blockage effect of the surface. As the surface becomes more flexible, the blockage effect is reduced and the increase becomes less significant. It is worth mentioning that at a flat free surface, the value of $(\partial\widetilde{w}/\partial\widetilde{z})^{rms}$ is $\sqrt{2}$ times that of $(\partial\widetilde{u}/\partial\widetilde{x})^{rms}$, which can be proved using the rapid distortion theory. The proof is given in Appendix B. This implies that the correlation between $\partial\widetilde{u}/\partial\widetilde{x}$ and $\partial\widetilde{v}/\partial\widetilde{y}$ is zero at the surface, because from continuity $(\partial\widetilde{w}/\partial\widetilde{z})^2 = (\partial\widetilde{u}/\partial\widetilde{x})^2 + (\partial\widetilde{v}/\partial\widetilde{y})^2 + 2(\partial\widetilde{u}/\partial\widetilde{x})(\partial\widetilde{v}/\partial\widetilde{y})$. For the cases simulated in the present study, it is found that the correlation coefficient between $\partial\widetilde{u}/\partial\widetilde{x}$ and $\partial\widetilde{v}/\partial\widetilde{y}$ at the free surface is very small (ranging from 0.0055 to 0.014). The surface values of $(\partial\widetilde{w}/\partial\widetilde{z})^{rms}/(\partial\widetilde{u}/\partial\widetilde{x})^{rms}$ are within 0.7 % error of $\sqrt{2}$. Therefore, the prediction of the rapid distortion theory is still valid for the surface deformations considered in the present study.

We next examine the variation of $(\partial\widetilde{w}/\partial\widetilde{x})^{rms}$ shown in figure 7(*c*). For the case of A1, which has the smallest surface deformation, $(\partial\widetilde{w}/\partial\widetilde{x})^{rms}$ decreases towards the surface as expected, because of the constraint of the surface on the vertical motion. As the free surface becomes more flexible, the reduction rate decreases (see the inset of figure 7*c*). For the case of C1, $(\partial\widetilde{w}/\partial\widetilde{x})^{rms}$ even increases slightly very close to the free surface, resulting in an appreciable surface value.

The behaviour of $(\partial\widetilde{u}/\partial\widetilde{z})^{rms}$ (figure 7*d*) is also interesting. Towards the surface, it increases first, reaches its maximum value at around $\widetilde{d} = -0.1$ and then decreases drastically over the region $\widetilde{d} > -0.1$. The first increase of $(\partial\widetilde{u}/\partial\widetilde{z})^{rms}$ is associated with the increase of $\widetilde{u}$ towards the surface discussed earlier (figure 7*d* also shows that when the surface becomes more flexible, the vertical variation of $(\partial\widetilde{u}/\partial\widetilde{z})^{rms}$ becomes less significant). As the surface is further approached, however, the shear-free DBC makes $\partial\widetilde{u}/\partial\widetilde{z} + \partial\widetilde{w}/\partial\widetilde{x}$ diminish. As a result, $\partial\widetilde{u}/\partial\widetilde{z}$ and $\partial\widetilde{w}/\partial\widetilde{x}$ are negatively correlated at the free surface, and their root-mean-square values are the same (shown in the insets of figure 7*c*,*d*). Because of the small surface value of $(\partial\widetilde{w}/\partial\widetilde{x})^{rms}$, $(\partial\widetilde{u}/\partial\widetilde{z})^{rms}$ has a sharp reduction over a thin near-surface region, which is the viscous layer (Hunt & Graham 1978; Walker *et al.* 1996; Shen *et al.* 1999).

The profile of $(\partial\widetilde{u}/\partial\widetilde{y})^{rms}$ is shown in figure 7(*e*). It does not change much as the free surface is approached, and the dependence on the surface deformation is relatively weak.

Having discussed the velocity gradients, we next examine the strain rate components $\widetilde{s}_{ij} = (\partial\widetilde{u}_i/\partial\widetilde{x}_j + \partial\widetilde{u}_j/\partial\widetilde{x}_i)/2$. It is straightforward to note the equivalence of $\widetilde{s}_{11}^{rms}$ and $\widetilde{s}_{22}^{rms}$ with $(\partial\widetilde{u}/\partial\widetilde{x})^{rms}$ and $\widetilde{s}_{33}^{rms}$ with $(\partial\widetilde{w}/\partial\widetilde{z})^{rms}$. Similar to $(\partial\widetilde{u}/\partial\widetilde{y})^{rms}$, the effect of the free surface on $\widetilde{s}_{12}^{rms}$ is small (results not shown here). Only $\widetilde{s}_{13}^{rms}$ ($\widetilde{s}_{23}^{rms}$ is the same) needs

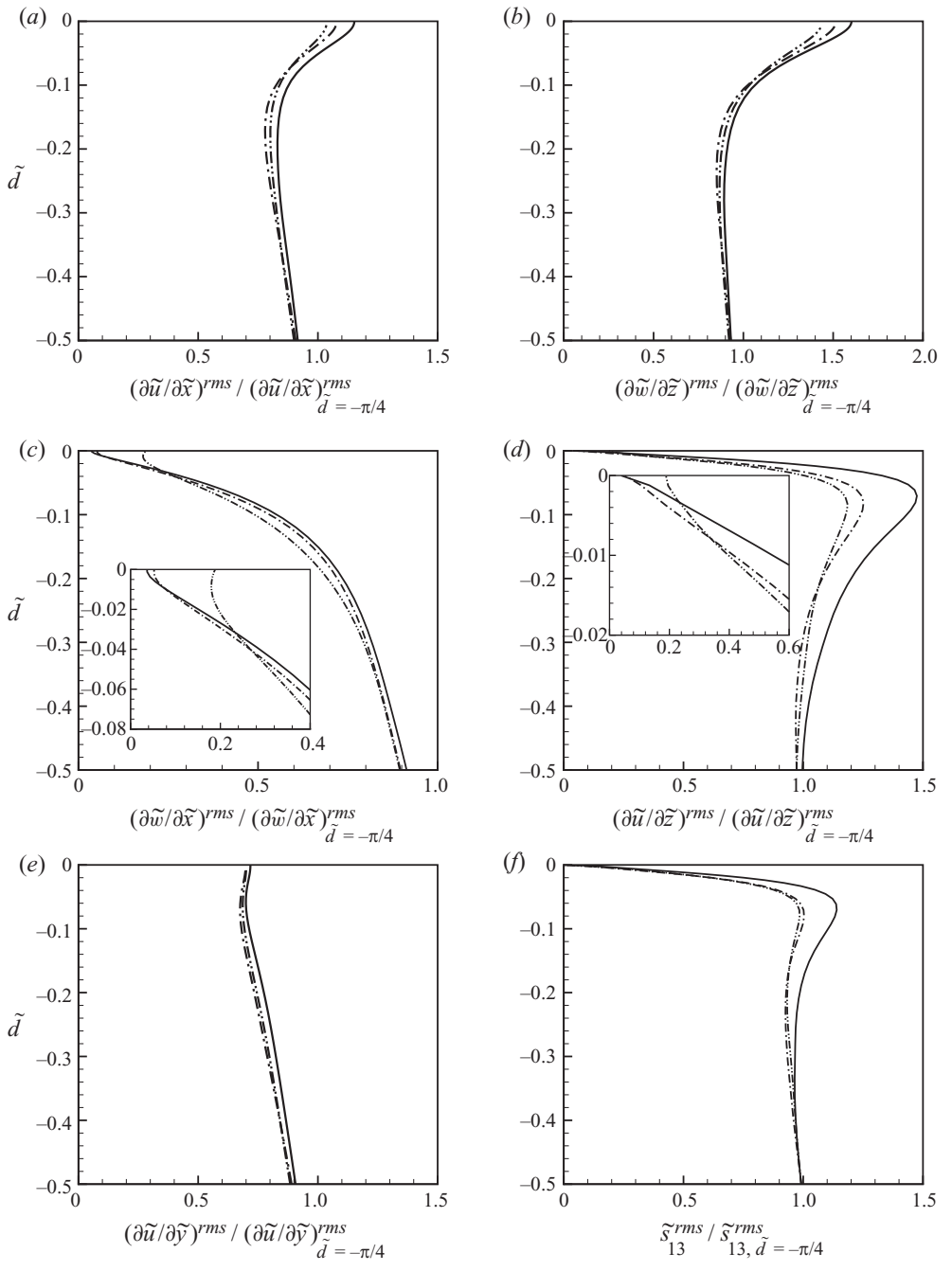

FIGURE 7. Normalized fluctuation profiles of (*a*) $\partial\tilde{u}/\partial\tilde{x}$, (*b*) $\partial\tilde{w}/\partial\tilde{z}$, (*c*) $\partial\tilde{w}/\partial\tilde{x}$, (*d*) $\partial\tilde{u}/\partial\tilde{z}$, (*e*) $\partial\tilde{u}/\partial\tilde{y}$ and (*f*) $\tilde{s}_{13}$. The insets in (*c*) and (*d*) show a zoom view of the near-surface region. ——, case A1; – · – · –, case B1; – · · – · · –, case C1.

discussion. As shown in figure 7(*f*), because of the shear-free boundary condition, $\tilde{s}^{rms}_{13}$ is zero at the free surface regardless of whether the surface is flexible or not. The vanishing of the surface-tangential shear stress has been regarded as the major reason for the reduction of viscous dissipation and thus the increase of turbulent kinetic

energy near a free surface (Perot & Moin 1995; Walker *et al.* 1996; Shen *et al.* 1999; Teixeira & Belcher 2000). For the deformable free surfaces considered in the present study, we did not find much change in the magnitude of the near-surface reduction of the dissipation. Therefore, the less significant increase of turbulent kinetic energy when the surface becomes more flexible, shown in figure 6(*c*), is caused by other reasons, which will be discussed in § 5.

4.3. *Budget of kinetic energy of horizontal and vertical turbulent motions*

In this section, we study the budget of turbulent kinetic energy for horizontal and vertical motions. The analysis is performed on the Cartesian coordinate system for the one-phase fluid below the intermittency layer. As pointed out earlier, the intermittency layer is very thin in the present study. The dynamics within the intermittency layer will be investigated in our future study for more suitable cases with much larger surface deformations.

The equations for the evolution of $\overline{u^2}$ and $\overline{w^2}$ are derived from the Navier–Stokes equations as (Tennekes & Lumley 1972)

$$\underbrace{\frac{\partial \overline{u^2}}{\partial t}}_{\mathrm{I}} = \underbrace{2\overline{p\frac{\partial u}{\partial x}}}_{\mathrm{II}} + \underbrace{\frac{1}{Re}\frac{\partial^2 \overline{u^2}}{\partial z^2}}_{\mathrm{III}} - \underbrace{\frac{2}{Re}\overline{\frac{\partial u}{\partial x_k}\frac{\partial u}{\partial x_k}}}_{\mathrm{IV}} - \underbrace{\frac{\partial}{\partial z}\overline{u^2 w}}_{\mathrm{V}}, \tag{4.1}$$

$$\underbrace{\frac{\partial \overline{w^2}}{\partial t}}_{\mathrm{I}} = \underbrace{2\overline{p\frac{\partial w}{\partial z}}}_{\mathrm{II}} + \underbrace{\frac{1}{Re}\frac{\partial^2 \overline{w^2}}{\partial z^2}}_{\mathrm{III}} - \underbrace{\frac{2}{Re}\overline{\frac{\partial w}{\partial x_k}\frac{\partial w}{\partial x_k}}}_{\mathrm{IV}} - \underbrace{\frac{\partial}{\partial z}\overline{w^3}}_{\mathrm{V}} - \underbrace{2\frac{\partial}{\partial z}\overline{pw}}_{\mathrm{VI}}. \tag{4.2}$$

Here the overline denotes the plane average on Cartesian coordinate. Term I is the rate of change in time, which is negligibly small because the flow is statistically steady. Term II is pressure–strain correlation; term III is viscous diffusion; term IV is viscous dissipation; term V is turbulent transport (caused by velocity fluctuations); and term VI is pressure-induced transport. Because there is no mean flow in the present problem, u_i is the same as u_i', and the superscript $'$ is omitted here. We also note that the production by the linear forcing does not show in (4.1) and (4.2), because the forcing is set to zero near the surface (2.2). Nevertheless, it should be pointed out that in the present problem, turbulence is generated in the bulk flow and is then transported to the near-surface region. Therefore, the process is different from the decaying turbulence case in Perot & Moin (1995) and Walker *et al.* (1996).

As shown in figure 8(*a*), far away from the free surface, the budget of $\overline{u^2}$ is dominated by two processes: velocity fluctuation transports energy from the turbulence generation region below towards the surface; meanwhile, $\overline{u^2}$ loses energy via the viscous dissipation.

As the free surface is approached, the other two terms become important too: the pressure–strain correlation is positive, corresponding to the energy transfer from the vertical velocity component to the horizontal ones; viscous diffusion has large negative value, indicating that $\overline{u^2}$ is transported from near the surface to the region below by molecular diffusion. Viscous dissipation continues to reduce $\overline{u^2}$. Towards the surface, its magnitude first increases slightly and then decreases. This variation is consistent with the viscous rapid distortion theory of Teixeira & Belcher (2000), the experimental result of Brumley & Jirka (1987) and the numerical results of Perot & Moin (1995), Walker *et al.* (1996) and Shen *et al.* (1999). Turbulent transport increases

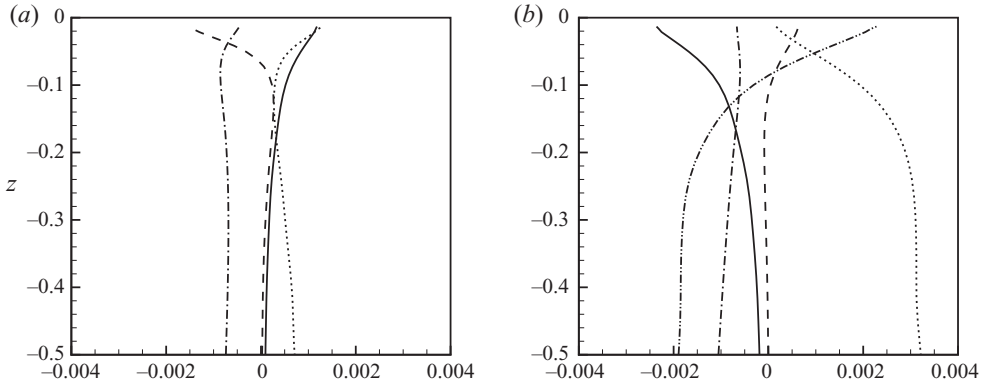

FIGURE 8. Budget terms in the evolution equations for (*a*) $\overline{u^2}$ and (*b*) $\overline{w^2}$. In both (*a*) and (*b*), ——, pressure–strain correlation; – – –, viscous diffusion; – · – · –, viscous dissipation; · · · · · ·, turbulent transport; – · · – · · –, pressure transport. The case of B1 is shown here.

sharply towards the free surface over the region $z > -0.1$. This corresponds to the upwelling in the near-surface region, which will be discussed in detail in § 5.1.

The budget for $\overline{w^2}$ is shown in figure 8(*b*). Away from the surface ($z < -0.1$), the budget of $\overline{w^2}$ is dominated by turbulent transport, viscous dissipation and pressure transport. As in the case of $\overline{u^2}$, $\overline{w^2}$ is transported from below by turbulent velocity fluctuation. In addition to viscous dissipation, pressure fluctuation also reduces $\overline{w^2}$ in the region below $z \approx -0.1$. The pressure transport term is absent in the $\overline{u^2}$ equation.

Close to the surface ($z > -0.1$), the pressure transport becomes positive and increases rapidly, indicating that pressure fluctuation plays an important role in the budget of $\overline{w^2}$. The transport associated with velocity fluctuation, on the other hand, decreases towards the surface because the vertical velocity is reduced by the surface blockage. The viscous diffusion is positive close to the surface. Because of the small value of $\overline{w^2}$ near the surface, molecular diffusion transports $\overline{w^2}$ from the region below to the near-surface region. The pressure–strain correlation term, which has been discussed in the $\overline{u^2}$ budget, transfers energy from the vertical motion to the horizontal. The magnitude of viscous dissipation for $\overline{w^2}$ remains about the same above $z = -0.1$, consistent with Brumley & Jirka (1987), Perot & Moin (1995), Walker *et al.* (1996) and Teixeira & Belcher (2000). As the surface is approached, $\partial w/\partial x$ and $\partial w/\partial y$ decrease, while $\partial w/\partial z$ increases (cf. figure 7). The net effect is that the $\overline{w^2}$ dissipation does not vary much near the surface.

In this section, only the result of case B1 is shown. Comparison with other cases for the effect of surface deformation will be discussed in § 5.3.

5. Contribution of splats and antisplats to $\overline{u^2}$ and $\overline{w^2}$ budget and effect of surface deformation

In § 4, we have discussed the flow anisotropy and the plane-averaged statistics of $\overline{u^2}$ and $\overline{w^2}$ budget. To gain more understanding on the physical process, in this section we study the effects of the coherent flow structures of splat (upwelling) and antisplat (downwelling), which are the characteristics of free-surface turbulence (see e.g. Pan & Banerjee 1995; Perot & Moin 1995).

5.1. *Variable interval spatial average results of splats*

We use conditional averaging to study splats first. The approach used in the present study is the variable interval spatial average (VISA) method (cf. Kim 1983; Jeong *et al.* 1997), with the surface divergence chosen as the detection variable. The sampling criterion is set to be the surface divergence being positive and its local maximum of variance exceeding five times the plane root-mean-square value. Details of our VISA procedure are given in Shen, Yue & Triantafyllou (2004). As in § 4.3, the analysis is performed on Cartesian coordinate below the intermittency layer.

Figure 9 shows the VISA results on a vertical cross-section passing the centre of the splat. The splat can be seen from the velocity vectors plotted in figure 9(*a*). We discuss pressure–strain correlation, turbulent transport and pressure transport, which are found to be strongly dependent on the splat.

As shown in figure 9(*a*), the pressure–strain correlation, $2\langle p\partial u/\partial x\rangle_{VISA}$, is maximum at the centre of the splat at the free surface, signifying energy redistribution from $\overline{w^2}$ to $\overline{u^2}$ there. Here $\langle\ \rangle_{VISA}$ denotes the conditional average result obtained from VISA. At the free surface, the energy redistribution occurs mainly over the region $-0.3 < x < 0.3$. In the vertical direction, the energy transfer occurs from the free surface down to $z = -0.1$, consistent with the pressure–strain correlation profile shown in figure 8.

Figure 9(*b*) shows that the turbulent transport of $\overline{u^2}$, $-\langle\partial u^2 w/\partial z\rangle_{VISA}$, is positive and maximum at the splat centre at the free surface. When a splat occurs a large amount of energy associated with the horizontal fluid motion is brought to the near-surface region by the vertical fluid motion. This result is consistent with figure 8. Figure 9(*b*) also shows that the shape and dimension of the turbulent transport region are relatively similar to those of the pressure–strain correlation.

Turbulent transport for $\overline{w^2}$, $-\langle\partial w^3/\partial z\rangle_{VISA}$, is also enhanced by splats (figure 9*c*). In contrast with the case of $-\langle\partial u^2 w/\partial z\rangle_{VISA}$, the maximum occurs below the surface, because the vertical velocity at the surface is greatly suppressed. For $\overline{w^2}$, pressure transport, $-2\langle\partial pw/\partial z\rangle_{VISA}$, also contributes to its increase at the splat region (figure 9*d*). The pressure transport has its negative centre around $z = -0.15$ and becomes positive around $z = -0.06$. Large pressure transport is located above the region of large turbulent transport. Therefore, for the energy associated with the vertical motion, both the turbulent velocity fluctuation and the pressure fluctuation contribute to the transport from the deep region towards the free surface. This result is again consistent with the plane-averaged profiles shown in figure 8.

To quantify the contribution of splats to the total energy budget, we define an effective area of splat events selected by the VISA method, using the criterion that the surface divergence is greater than half of the plane root-mean-square value. It is found that with only 9.0 % of the area of the $z = -2\eta^{rms}$ plane close to the free surface, the integrated value of $2\langle p\partial u/\partial x\rangle_{VISA}$, $-\langle\partial u^2 w/\partial z\rangle_{VISA}$ and $-2\langle\partial pw/\partial z\rangle_{VISA}$ are respectively 121 %, 145 % and 118 % of the integrals over the whole plane, signifying the dominant role played by the splats. Note that the values larger than 100 % means that they are offset by the counter-effect at non-splat regions.

To show the effect of splats on flow anisotropy, we plot $\langle u^2\rangle_{VISA}$ and $\langle w^2\rangle_{VISA}$ in figure 9(*e*,*f*). At the splat, the vertical motion below the surface is effectively turned into the horizontal direction near the free surface. Under the action of the pressure–strain correlation and the turbulent transport (figure 9*a*, *b*), $\langle u^2\rangle_{VISA}$ reaches its maximum value around $x = \pm 0.22$ at the surface.

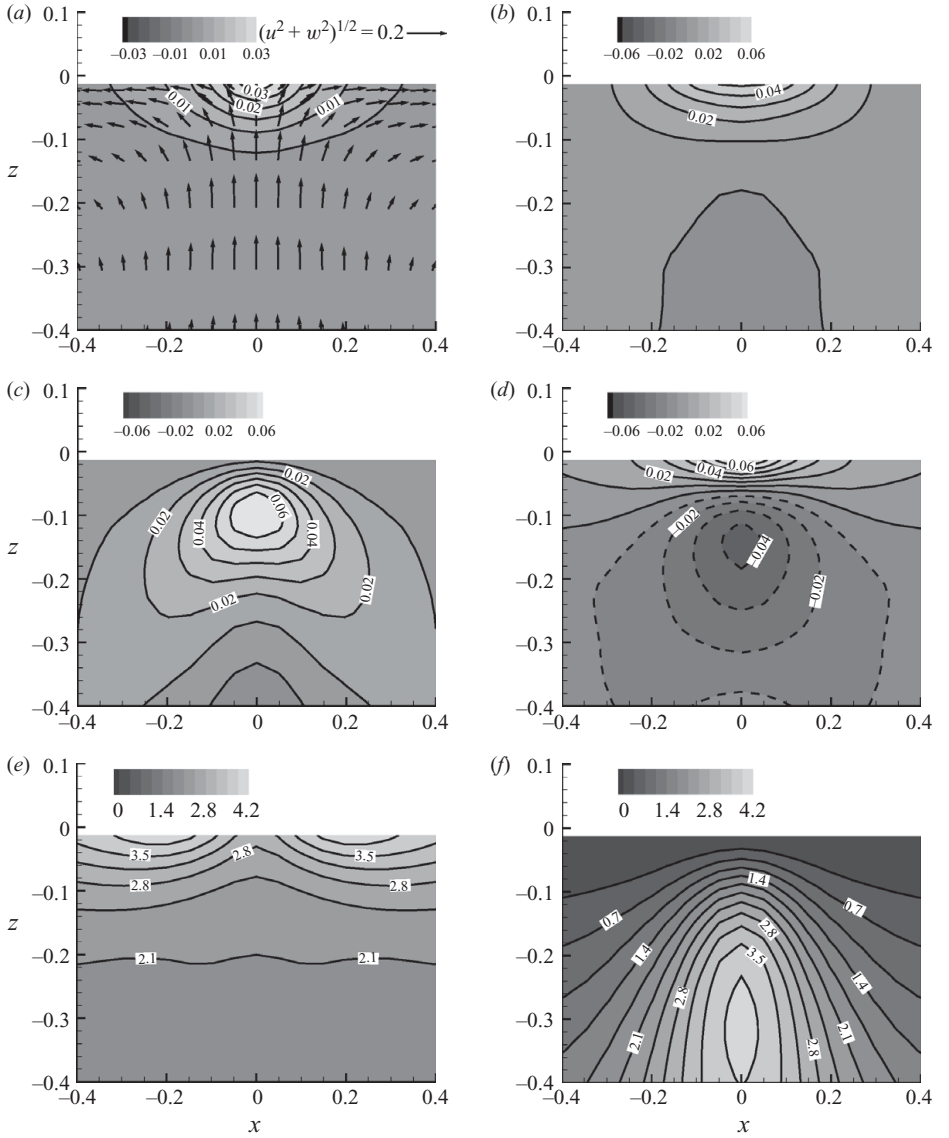

FIGURE 9. VISA results of splats. On the vertical cross-section passing the splat centre, contours of (*a*) pressure–strain correlation $2\langle p\partial u/\partial x\rangle_{VISA}$, (*b*) turbulent transport $-\langle\partial u^2 w/\partial z\rangle_{VISA}$, (*c*) turbulent transport $-\langle\partial w^3/\partial z\rangle_{VISA}$, (*d*) pressure transport $-2\langle\partial pw/\partial z\rangle_{VISA}$, (*e*) $\langle u^2\rangle_{VISA}$ and (*f*) $\langle w^2\rangle_{VISA}$ are plotted. In (*a*), the velocity vectors are shown at every four grid points in the vertical direction for better visualization. In (*e*) and (*f*), the results are normalized by the corresponding plane-averaged values at $z = -\pi/4$, where the flow is nearly isotropic. The case of B1 is shown here.

5.2. *VISA results of antisplats*

Next, we use VISA to analyse antisplats. The procedure is the same as in the splat case, the only change being that the sampling is now for negative instead of positive surface divergence. However, it should be emphasized that the splats and the antisplats are very different in their instantaneous appearance (cf. Pan & Banerjee 1995, figure 5;

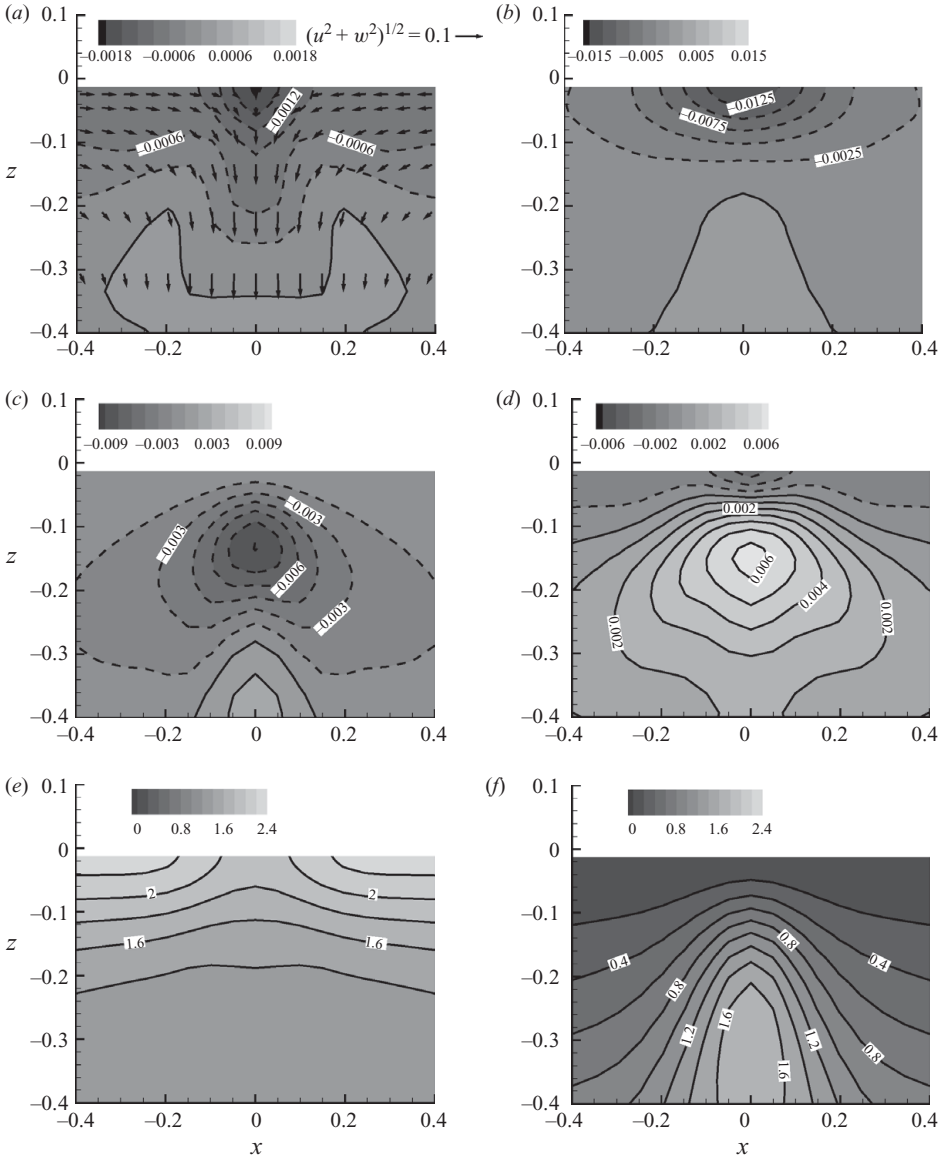

FIGURE 10. VISA results of antisplats. The notation is the same as in figure 9.

Perot & Moin 1995, figure 8; Shen *et al.* 2004, figure 5). Unlike splats, which usually have a simple round shape on the surface, antisplats are often distributed over a long and narrow band with a highly irregular geometry. After the VISA averaging over many antisplat structures with different orientations, the conditionally averaged flow field becomes isotropic. Therefore, caution must be taken not to mistake the round structure in the VISA field for the geometry of the individual antisplats, which is much more complex (this is not a concern for splats because of the relatively simple geometry of their individual appearance). The results in this section are for the statistics of the average effect of the antisplats, not for the study of their topology.

Figure 10 plots the VISA results of the antisplats. The velocity vectors in figure 10(*a*) indicate clearly the transfer from horizontal to vertical motions. As for splats, it is

found that the pressure–strain correlation and the turbulent transport play an essential role in the $\overline{u^2}$ budget; for the $\overline{w^2}$ budget, in addition to these two terms, pressure transport is also important. It should be noted that these terms are of opposite sign to those in the splat case.

Figure 10(a) plots the pressure–strain correlation term, $2\langle p\partial u/\partial x\rangle_{VISA}$. It is negative near the free surface, indicating that there is energy redistribution from $\overline{u^2}$ to $\overline{w^2}$. This effect offsets the energy transfer from the vertical to horizontal motions occurring at the splats. Distribution of the turbulent transport for $\overline{u^2}$, namely $-\langle\partial u^2 w/\partial z\rangle_{VISA}$, is plotted in figure 10(b). It is negative near the free surface, corresponding to the transport of $\overline{u^2}$ from the near-surface region to the region below.

For $\overline{w^2}$, in addition to the pressure–strain correlation $2\langle p\partial w/\partial z\rangle_{VISA}$ (not plotted because it can be deduced from $2\langle p\partial u/\partial x\rangle_{VISA}$ in figure 10a), the transport caused by pressure and velocity fluctuations also plays an important role in the budget of $\overline{w^2}$ near the free surface. Figure 10(d) shows that the pressure transport $-2\langle\partial pw/\partial z\rangle_{VISA}$ is negative very close to the surface, while figure 10(c) shows that the turbulent transport $-\langle\partial w^3/\partial z\rangle_{VISA}$ has significant negative values some distance below the surface. They together transport $\overline{w^2}$, which is gained from $\overline{u^2}$ through the pressure–strain correlation, from the near-surface region to the deep region.

As in the splat case, we define an effective area for the antisplats selected for the conditional average. These antisplat events occupy 8.6 % of the horizontal plane at $z=-2\eta^{rms}$. Their contributions to the pressure–strain correlation, the turbulent transport for $\overline{u^2}$, and the pressure transport for $\overline{w^2}$ over the entire plane are -19 %, -38 % and -18 %, respectively. All these percentage numbers have the minus sign, because their role is to offset the overall energy transfer that mainly occurs at the splats shown earlier.

Finally, $\langle u^2\rangle_{VISA}$ and $\langle w^2\rangle_{VISA}$ are shown in figure 10(e,f). The $\langle u^2\rangle_{VISA}$ is maximum at the surface away from the antisplat core, corresponding to the large inward horizontal motion. At the antisplat, the horizontal motion is turned into the vertical direction, resulting in enhanced $\langle w^2\rangle_{VISA}$ below the surface. This process counters that in the splat case.

5.3. *Dependence on surface deformation*

In §§ 5.1 and 5.2, it is shown that splats and antisplats strongly affect the pressure–strain correlation and transport in the budget of $\overline{u^2}$ and $\overline{w^2}$. We next discuss the effect of surface deformation on these processes. It is noted that to show comparison, results for different cases can be plotted in the same way as in figures 9 and 10. Alternatively, we adopt here a more compact way, used in Shen *et al.* (1999) to show the surface distributions of the budget terms conditioned upon the quantity

$$D_n \equiv \frac{(\partial u/\partial x+\partial v/\partial y)\,/(\partial u/\partial x+\partial v/\partial y)^{rms}}{q/q^{rms}}. \tag{5.1}$$

Here $q=(u^2+v^2+w^2)^{1/2}$. The representation using D_n can indicate different stages of the splat and antisplat processes effectively. At the centre of splats, the surface divergence $\partial u/\partial x+\partial v/\partial y$ is large, while q is small near the stagnation point. As a result, D_n has large positive values. For the same reason, it has large negative values at the core of antisplats. In between splats and antisplats, $\partial u/\partial x+\partial v/\partial y$ is small while q is large because of along-surface fluid motions, resulting in small values of D_n. We use $\langle\ \rangle_{cond}$ to denote the results conditioned on D_n.

Figure 11 plots the surface values of the pressure–strain correlation and the turbulent transport for $\overline{u^2}$ as functions of D_n. As shown, $\langle 2p\partial u/\partial x\rangle_{cond}$ is positive

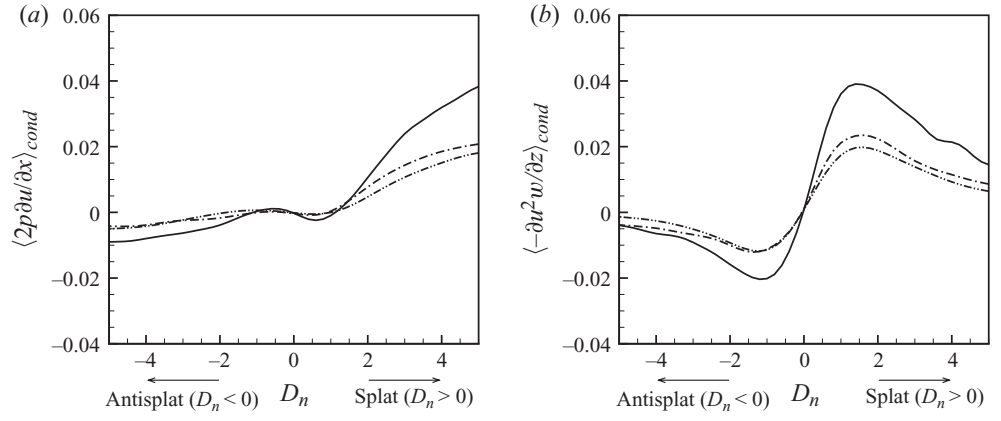

FIGURE 11. Variations of (*a*) pressure–strain correlation $\langle 2p\partial u/\partial x\rangle_{cond}$, and (*b*) turbulent transport $\langle -\partial u^2 w/\partial z\rangle_{cond}$ as functions of D_n during the splat and antisplat processes for the cases of: ——, A1; – · – · –, B1; – · · – · · –, C1.

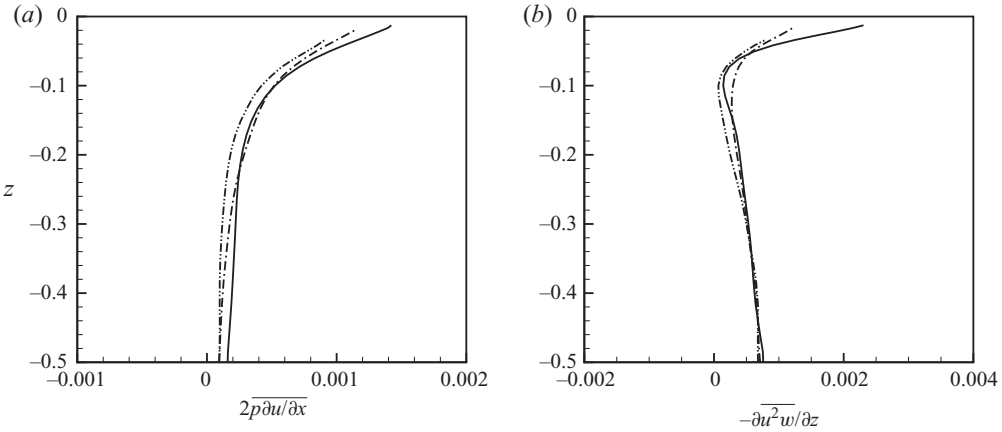

FIGURE 12. Profiles of (*a*) pressure–strain correlation $2\overline{p\partial u/\partial x}$, and (*b*) turbulent transport $-\overline{\partial u^2 w/\partial z}$: ——, case A1; – · – · –, case B1; – · · – · · –, case C1.

at splats and negative at antisplats, consistent with figures 9(*a*) and 10(*a*). We note that the variation in the splat and antisplat regions is not symmetric in figure 11(*a*), with the antisplat side being weaker. As pointed out by Perot & Moin (1995), after a splat event, the fluid motion along the surface is dissipated by viscosity before an antisplat occurs. It is the imbalance between splats and antisplats that results in the net inter-component energy transfer from $\overline{w^2}$ to $\overline{u^2}$.

Figure 11(*a*) shows that as *Fr* increases, the surface blockage effect and hence the pressure–strain correlation are reduced significantly. Shen *et al.* (1999) found that even a small value of *Fr* can cause noticeable difference from the flat-surface case in pressure–strain correlation. The results obtained here further show that the surface deformation can affect the pressure–strain correlation significantly. Figure 12(*a*) shows the vertical profile of the plane-averaged statistics $2\overline{p\partial u/\partial x}$ (plotted up to $z = -2\eta^{rms}$ as in §4.3) for the cases of A1, B1 and C1, which shows the reduction in magnitude as *Fr* increases.

The surface distribution of the turbulent transport term for $\overline{u^2}$, $\langle -\partial u^2 w/\partial z\rangle_{cond}$, is plotted in figure 11(b). It is positive over the splat region and negative over the antisplat region, consistent with the results shown in figures 9(b) and 10(b). We also note that the upward transport in the splat region is larger than the downward transport in the antisplat region. As shown in figure 8(a), the overall effect is that $\overline{u^2}$ is transported from the flow below to the near-surface region.

We note that turbulent transport $\langle -\partial u^2 w/\partial z\rangle_{cond}$ does not vary with D_n monotonically. On the splat side, as D_n increases, the turbulent transport increases to a maximum value around $D_n = 1$ and then decreases. Similarly, on the antisplat side, the minimum occurs around $D_n = -1$. This phenomenon can be understood as follows. At the free surface, the main contribution to $\langle -\partial u^2 w/\partial z\rangle_{cond}$ is $\langle -u^2 \partial w/\partial z\rangle_{cond} = \langle u^2(\partial u/\partial x + \partial v/\partial y)\rangle_{cond}$. For it to be significant, both u and $\partial u/\partial x + \partial v/\partial y$ need to be large. From the definition of D_n, we see that a large D_n value occurs when $\partial u/\partial x + \partial v/\partial y$ is large but u is small. Only at an intermediate value of D_n does the combined effect of $\partial u/\partial x + \partial v/\partial y$ and u make the turbulent transport maximum.

Comparing the different curves in figure 11(b), we see the turbulent transport is sensitive to the surface deformation. As Fr increases, the magnitude of the turbulent transport decreases. This can also be seen in the comparison of the plane-averaged statistics $-\partial\overline{u^2 w}/\partial z$ among cases A1, B1 and C1 plotted in figure 12(b).

Figure 11 is for the $\overline{u^2}$ budget. For $\overline{w^2}$, the corresponding terms can be deduced from the $\overline{u^2}$ results, and are not plotted separately here. The pressure–strain correlation $\langle 2p\partial w/\partial z\rangle_{cond}$ can be deduced from $\langle 2p\partial u/\partial x\rangle_{cond}$ shown in figure 11(a). The turbulent transport $\langle -\partial w^3/\partial z\rangle_{cond}$ at the free surface is negligibly small because of the small vertical motion there. We also note that for $\overline{w^2}$, at the free surface, the pressure–strain correlation term is nearly balanced by the pressure transport term (see (4.2) and figure 8b). The roles of pressure–strain correlation and pressure transport in the near-surface $\overline{w^2}$ evolution can be summarized as follows: over the splat region, the energy loss of $\overline{w^2}$ (to $\overline{u^2}$) via the pressure–strain correlation is supplied by the pressure transport of $\overline{w^2}$ from below; and over the antisplat region, the energy gain of $\overline{w^2}$ (from $\overline{u^2}$) is transported away through the pressure transport. This result is consistent with the discussion in §§ 5.1 and 5.2.

The above-discussed result shows the effect of surface deformation, which is important for the understanding of the difference in the turbulent kinetic energy among different cases shown in figure 6. For a flat free surface, the increase of the kinetic energy towards the surface has been attributed to the reduction of viscous dissipation owing to the vanishing of surface-tangential stress (Perot & Moin 1995; Walker *et al.* 1996; Shen *et al.* 1999; Teixeira & Belcher 2000). When the surface is deformable, the vanishing of shear stress still holds in the local surface-tangential directions. As a result, we do not observe much change in the viscous dissipation when the surface flexibility increases. Alternatively, it is the pressure–strain correlation and turbulent transport of $\overline{u^2}$ that are reduced noticeably as the surface deformation increases, as shown in this section. As a result, the near-surface accumulation of $\overline{u^2}$ and hence the kinetic energy (figure 6) becomes less significant compared with the flat-surface case. Finally, we note that the above explanation still holds if viewed from the total kinetic energy directly, because the pressure–strain correlation for horizontal velocities is balanced by that for the vertical velocity, while the latter is again nearly balanced by the pressure transport at the free surface as discussed earlier (in other words, from the viewpoint of the budget for the turbulent kinetic energy, it would be

the transport due to velocity and pressure fluctuations that causes the variation of turbulent kinetic energy at the surface).

6. Conclusions

In this study, we have used DNS to investigate the interaction between a deformable free surface and a homogeneous turbulent flow below. We use a linear forcing method to generate statistically steady, isotropic turbulence in the bulk flow. This problem setting has the theoretical advantage of being simple and fundamental, and it corresponds to laboratory experiments using tanks with stirring grids or random jets. To the best of our knowledge, this is the first time such a configuration has been set up in numerical simulation (before this, the closest numerical simulation in the literature was decaying isotropic turbulence being suddenly inserted with a free-slip plate). The present study serves as the first step towards a comprehensive understanding of this type of canonical problem.

It is found that the surface deformation is characterized by propagating waves and turbulence-induced roughness, which are shown in the frequency–wavenumber spectrum of the surface elevation. The waves are manifested mainly at low wavenumbers by the correspondence to the dispersion relationship. The turbulence-induced roughness appears at all wavenumbers. Its motion can be approximately represented by a characteristic frequency using the free-surface nonlinear KBC. For the cases considered in this study, the surface potential energy is 23.4–38.3 % of the kinetic energy contained in the intermittency layer. Of the potential energy, a small fraction (ranging from 2.2 % to 12.1 % in our simulation cases) is associated with waves. Through simulations of cases with different Froude and Weber numbers, we have also shown the roles of gravity and surface tension in the surface deformation. Their relative importance is related to a critical wavenumber that is defined on the basis of the *Fr* and *We* values. For the current problem, most of the surface potential energy (91.6–98.6 %) is associated with the gravity. The surface tension effect becomes dominant at high wavenumbers, and it affects the smoothness of the surface.

To study the effect of the free surface on the turbulence underneath, we have examined the fluctuations of velocity, velocity gradients and strain rate in the vicinity of the free surface. Their surface-normal and surface-tangential components are investigated as functions of the distance to the free surface. Effects of both the blockage effect and the vanishing of shear stress at the surface on the flow anisotropy are shown. It is found that compared with a flat shear-free surface, the surface deformation may make a noticeable difference to some of the turbulence statistics. For example, the horizontal velocity fluctuation increases by about 45 % towards a flat surface, while it increases by only 20 % in the case of C1, which has the largest surface deformation in our study. For the horizontal and vertical turbulent motions, we have studied their energy budget on a Cartesian coordinate system. It is found that for $\overline{u^2}$, the turbulent velocity fluctuation transports energy from the bulk flow towards the free surface. Near the surface, $\overline{u^2}$ gains energy from $\overline{w^2}$ through pressure–strain correlation. Viscous dissipation decreases towards the free surface. Viscous diffusion transports $\overline{u^2}$ from the near-surface region to the lower region. For $\overline{w^2}$, in addition to the turbulent velocity fluctuation, pressure fluctuation also plays an important role in the transport process. Because $\overline{w^2}$ decreases towards the free surface, viscous diffusion contributes to the transport of energy to the near-surface region, which is offset by viscous dissipation at the free surface.

To further gain insights into the inter-component transport and transfer processes of turbulent kinetic energy near the free surface, we have performed VISA conditional averaging for the characteristic flow structures of splat and antisplat to show their importance. In our VISA, although splats occupy only 9 % of the area of the $z=-2\eta^{rms}$ plane close to the surface, they contribute to respectively 121 %, 145 % and 118 % of the total values of pressure–strain correlation, turbulent transport for $\overline{u^2}$ and pressure transport for $\overline{w^2}$ over the entire plane. Antisplats that occupy 8.6 % of the area, on the other hand, offset respectively 19 %, 38 % and 18 % of these terms. Finally, we have used conditional averaging on the basis of the splat and antisplat processes to show that the surface deformation affects the pressure–strain correlation and the transport appreciably, which reduces the accumulation of horizontal velocity fluctuations and turbulent kinetic energy at the free surface compared with the flat-surface case.

Support by the Office of Naval Research on this research is gratefully acknowledged. We would also like to thank the referees for their valuable comments, which gave us significant help in improving the previous version of this paper.

Appendix A. Projection to the local surface-normal and surface-tangential directions

Let $\widetilde{d}$ denote the signed distance from the free surface, with the minus sign corresponding to the waterside. Following Kang, Fedkiw & Liu (2000), for any spatial point with $\widetilde{d}$, we define the unit vector normal to the iso-surface of $\widetilde{d}$ as

$$\widetilde{\boldsymbol{e}}_3=\frac{\nabla\widetilde{d}}{|\nabla\widetilde{d}|}, \tag{A 1}$$

and the two unit vectors tangential to the iso-surface of $\widetilde{d}$ as

$$\widetilde{\boldsymbol{e}}_1=\frac{(0,1,0)\times\widetilde{\boldsymbol{e}}_3}{|(0,1,0)\times\widetilde{\boldsymbol{e}}_3|}, \quad \widetilde{\boldsymbol{e}}_2=\widetilde{\boldsymbol{e}}_3\times\widetilde{\boldsymbol{e}}_1. \tag{A 2}$$

We note that the choice of $\widetilde{\boldsymbol{e}}_1$ and $\widetilde{\boldsymbol{e}}_2$ is not unique. For the current problem, there is no preference for their choice because of the horizontal isotropy; here we choose $\widetilde{\boldsymbol{e}}_1$ to be on the (x,z) plane simply for convenience.

We project a vector $\boldsymbol{B}$ (such as velocity and vorticity) and a tensor $[\boldsymbol{s}]$ (such as stress and strain rate) to the directions of $\widetilde{\boldsymbol{e}}_1$, $\widetilde{\boldsymbol{e}}_2$ and $\widetilde{\boldsymbol{e}}_3$ as

$$\widetilde{B}_i=\beta_{ij}B_j, \qquad \widetilde{s}_{ij}=s_{mn}\beta_{im}\beta_{jn}. \tag{A 3}$$

Here the tilde denotes the projected quantities; and $\beta_{ij}=\widetilde{\boldsymbol{e}}_i\cdot\widetilde{\boldsymbol{e}}_j$. In the present study, statistics are performed over the iso-surface of $\widetilde{d}$. Linear interpolation is used when data are transformed from the discrete computational grid.

Appendix B. Analysis of $(\partial u/\partial x)^{rms}$ and $(\partial w/\partial z)^{rms}$ at a flat free surface using the rapid distortion theory

On the basis of the rapid distortion theory analyses by Hunt & Graham (1978) and Teixeira & Belcher (2000), the variances of velocity derivatives can be obtained as follows.

(*a*) Velocity derivatives in the horizontal directions:

$$\overline{\left(\frac{\partial u_i}{\partial x_\alpha}\right)^2} = \iiint k_\alpha^2 M_{ik}^*(\boldsymbol{k}, z, t)\, M_{il}(\boldsymbol{k}, z, t)\, \Phi_{kl}^{(H)}\, \mathrm{d}k_1\, \mathrm{d}k_2\, \mathrm{d}k_3. \tag{B 1}$$

(*b*) Velocity derivatives in the vertical direction:

$$\overline{\left(\frac{\partial u_i}{\partial z}\right)^2} = \iiint \frac{\partial M_{ik}^*(\boldsymbol{k}, z, t)}{\partial z} \frac{\partial M_{il}(\boldsymbol{k}, z, t)}{\partial z} \Phi_{kl}^{(H)}\, \mathrm{d}k_1\, \mathrm{d}k_2\, \mathrm{d}k_3. \tag{B 2}$$

Here, $i = 1, 2$ or 3; $\alpha = 1$ or 2; the superscript '$*$' denotes the complex conjugate. Near the free surface, because the variation of $(\partial u/\partial x)^{rms}$ and $(\partial w/\partial z)^{rms}$ is mainly caused by the blockage effect of the surface (i.e. the viscous correction is relatively weak; cf. Teixeira & Belcher 2000), we use the matrix M_{ij} of Hunt & Graham (1978) for simplicity:

$$\left.\begin{aligned} M_{\alpha\alpha} &= \mathrm{e}^{\mathrm{i}k_3 z} \qquad \text{(no summation on } \alpha\text{)},\\ M_{\alpha 3} &= \frac{\mathrm{i}k_\alpha}{\sqrt{k_1^2 + k_2^2}} \mathrm{e}^{-\sqrt{k_1^2 + k_2^2}\, z},\\ M_{33} &= \mathrm{e}^{\mathrm{i}k_3 z} - \mathrm{e}^{-\sqrt{k_1^2 + k_2^2}\, z}. \end{aligned}\right\} \tag{B 3}$$

The remaining components of M_{ij} are zero. In (B 1) and (B 2), $\Phi_{ij}^{(H)}$ is the velocity spectrum of the undistorted isotropic, homogeneous turbulence underneath (cf. Hinze 1959; Teixeira & Belcher 2000):

$$\Phi_{ij}^{(H)} = \left(\delta_{ij} - \frac{k_i k_j}{k^2}\right) \frac{E(k)}{4\pi k^2}, \tag{B 4}$$

where $k = \sqrt{k_1^2 + k_2^2 + k_3^2}$ and $E(k)$ is the turbulence energy spectrum underneath. Substituting (B 3) and (B 4) into (B 1) and (B 2) and taking the limit of z approaching zero, we obtain

$$\left.\begin{aligned} \overline{\left(\frac{\partial u_\alpha}{\partial x_\alpha}\right)^2} &= \iiint k_1^2 \frac{E(k)}{4\pi}\, \mathrm{d}k_1\, \mathrm{d}k_2\, \mathrm{d}k_3 \qquad \text{(no summation on } \alpha\text{)},\\ \overline{\left(\frac{\partial w}{\partial z}\right)^2} &= \iiint \left(k_1^2 + k_2^2\right) \frac{E(k)}{4\pi}\, \mathrm{d}k_1\, \mathrm{d}k_2\, \mathrm{d}k_3. \end{aligned}\right\} \tag{B 5}$$

Comparing the two equations in (B 5) and using the fact that the flow is horizontally isotropic, we conclude that $\overline{(\partial w/\partial z)^2}$ is twice $\overline{(\partial u/\partial x)^2}$ at a flat free surface. Therefore, the surface value of $(\partial u/\partial x)^{rms}$ is $\sqrt{2}$ times that of $(\partial w/\partial z)^{rms}$.

REFERENCES

Borue, V., Orszag, S. A. & Staroselsky, I. 1995 Interaction of surface waves with turbulence: direct numerical simulations of turbulent open-channel flow. *J. Fluid Mech.* **286**, 1–23.

Brocchini, M. 2002 Free surface boundary conditions at a bubbly/weakly splashing air–water interface. *Phys. Fluids* **14**, 1834–1840.

Brocchini, M. & Peregrine, D. H. 2001 The dynamics of strong turbulence at free surfaces. Part 2. Free-surface boundary conditions. *J. Fluid Mech.* **449**, 255–290.

Brumley, B. H. & Jirka, G. H. 1987 Near-surface turbulence in a grid-stirred tank. *J. Fluid Mech.* **183**, 235–263.

Calmet, I. & Magnaudet, J. 2003 Statistical structure of high-Reynolds-number turbulence close to the free surface of an open-channel flow. *J. Fluid Mech.* **474**, 355–378.

Dabiri, D. & Gharib, M. 2001 Simultaneous free-surface deformation and near-surface velocity measurements. *Exp. Fluids* **30**, 381–390.

Dimas, A. A. & Triantafyllou, G. S. 1994 Nonlinear interaction of shear flow with a free surface. *J. Fluid Mech.* **260**, 211–246.

Dommermuth, D. G. 1994 The initialization of vortical free-surface flows. *J. Fluids Engng* **116**, 95–102.

Dopazo, C., Lozano, A. & Barreras, F. 2000 Vorticity constraints on a fluid/fluid interface. *Phys. Fluids* **12**, 1928–1931.

Guo, X. 2010 Simulation-based study of turbulence interacting with a deformable free surface. Master's thesis, Johns Hopkins University, Baltimore, MD.

Guo, X. & Shen, L. 2009 On the generation and maintenance of waves and turbulence in simulations of free-surface turbulence. *J. Comput. Phys.* **228**, 7313–7332.

Handler, R. A., Swean Jr., T. F., Leighton, R. I. & Swearingen, J. D. 1993 Length scales and the energy balance for turbulence near a free surface. *AIAA J.* **31**, 1998–2007.

Harlow, F. H. & Welch, J. E. 1965 Numerical calculation of time-dependent viscous incompressible flow of fluid with free surface. *Phys. Fluids* **8**, 2182–2189.

Herlina & Jirka, G. H. 2008 Experiments on gas transfer at the air–water interface induced by oscillating grid turbulence. *J. Fluid Mech.* **594**, 183–208.

Hinze, J. O. 1959 *Turbulence*. McGraw-Hill.

Hodges, B. R. & Street, R. L. 1999 On simulation of turbulent nonlinear free-surface flows. *J. Comput. Phys.* **151**, 425–457.

Hong, W.-L. & Walker, D. T. 2000 Reynolds-averaged equations for free-surface flows with application to high-Froude-number jet spreading. *J. Fluid Mech.* **417**, 183–209.

Hunt, J. C. R. 1984 Turbulence structure in thermal convection and shear-free boundary layers. *J. Fluid Mech.* **138**, 161–184.

Hunt, J. C. R. & Graham, J. M. R. 1978 Free-stream turbulence near plane boundaries. *J. Fluid Mech.* **84**, 209–235.

Jeong, J., Hussain, F., Schoppa, W. & Kim, J. 1997 Coherent structures near the wall in a turbulent channel flow. *J. Fluid Mech.* **332**, 185–214.

Kang, M., Fedkiw, R. P. & Liu, X.-D. 2000 A boundary condition capturing method for multiphase incompressible flow. *J. Sci. Comput.* **15**, 323–360.

Kim, J. 1983 On the structure of wall-bounded turbulent flows. *Phys. Fluids* **26**, 2088–2097.

Kim, J. & Moin, P. 1985 Application of a fractional-step method to incompressible Navier–Stokes equations. *J. Comput. Phys.* **59**, 308–323.

Kitaigorodskii, S. A. & Lumley, J. L. 1983 Wave–turbulence interactions in the upper ocean. Part I. The energy balance of the interacting fields of surface wind waves and wind-induced three-dimensional turbulence. *J. Phys. Oceanogr.* **13**, 1977–1987.

Komori, S., Nagaosa, R., Murakami, Y., Chiba, S., Ishii, K. & Kuwahara, K. 1993 Direct numerical simulation of three-dimensional open-channel flow with zero-shear gas–liquid interface. *Phys. Fluids* A **5**, 115–125.

Kumar, S., Gupta, R. & Banerjee, S. 1998 An experimental investigation of the characteristics of free-surface turbulence in channel flow. *Phys. Fluids* **10**, 437–456.

Lam, K. & Banerjee, S. 1988 Investigation of turbulent flow bounded by a wall and a free surface. In *Fundamentals of Gas–Liquid Flows* (ed. E. E. Michaelides & M. P. Sharma), pp. 29–38. ASME.

Leighton, R. I., Swean Jr., T. F., Handler, R. A. & Swearingen, J. D. 1991 Interaction of vorticity with a free surface in turbulent open channel flow. *Paper 91–0236*. AIAA.

Longuet-Higgins, M. S. 1998 Vorticity and curvature at a free surface. *J. Fluid Mech.* **356**, 149–153.

Lugt, H. J. 1987 Local flow properties at a viscous free surface. *Phys. Fluids* **30**, 3647–3652.

Lundgren, T. 2003 Linearly forced isotropic turbulence. *Tech. Rep.* 461. Center for Turbulence Research, Stanford, CA.

Lundgren, T. & Koumoutsakos, P. 1999 On the generation of vorticity at a free surface. *J. Fluid Mech.* **382**, 351–366.

Magnaudet, J. 2003 High-Reynolds-number turbulence in a shear-free boundary layer: revisiting the Hunt–Graham theory. *J. Fluid Mech.* **484**, 167–196.

McKenna, S. P. & McGillis, W. R. 2004 The role of free-surface turbulence and surfactants in air–water gas transfer. *Intl J. Heat Mass Transfer* **47**, 539–553.

Nagaosa, R. 1999 Direct numerical simulation of vortex structures and turbulent scalar transfer across a free surface in a fully developed turbulence. *Phys. Fluids* **11**, 1581–1595.

Nagaosa, R. & Handler, R. A. 2003 Statistical analysis of coherent vortices near a free surface in a fully developed turbulence. *Phys. Fluids* **15**, 375–394.

Nielsen, P. & Skovgaard, O. 1990 The effect of using non-orthogonal boundary-fitted grids for solving the shallow water equations. *Intl J. Numer. Methods Fluids* **11**, 177–188.

Olmez, H. S. & Milgram, J. H. 1992 An experimental study of attenuation of short water waves by turbulence. *J. Fluid Mech.* **239**, 133–156.

Pan, Y. & Banerjee, S. 1995 A numerical study of free-surface turbulence in channel flow. *Phys. Fluids* **7**, 1649–1664.

Perot, B. & Moin, P. 1995 Shear-free turbulent boundary layers. Part 1. Phyiscal insights into near-wall turbulence. *J. Fluid Mech.* **295**, 199–227.

Phillips, O. M. 1958 The equilibrium range in the spectrum of wind-generated waves. *J. Fluid Mech.* **4**, 426–434.

Rashidi, M. 1997 Burst-interface interactions in free surface turbulent flows. *Phys. Fluids* **9**, 3485–3501.

Rosales, C. & Meneveau, C. 2005 Linear forcing in numerical simulations of isotropic turbulence: physical space implementations and convergence properties. *Phys. Fluids* **17**, 095106.

Sankaranarayanan, S. & Spaulding, M. L. 2003 A study of the effects of grid non-orthogonality on the solution of shallow water equations in boundary-fitted coordinate systems. *J. Comput. Phys.* **184**, 299–320.

Sarpkaya, T. 1996 Vorticity, free surface, and surfactants. *Annu. Rev. Fluid. Mech.* **28**, 83–128.

Savelsberg, R. & van de Water, W. 2009 Experiments on free-surface turbulence. *J. Fluid Mech.* **619**, 95–125.

Shen, L., Triantafyllou, G. S. & Yue, D. K. P. 2000 Turbulent diffusion near a free surface. *J. Fluid Mech.* **407**, 145–166.

Shen, L., Yue, D. K. P. & Triantafyllou, G. S. 2004 Effect of surfactants on free-surface turbulent flows. *J. Fluid Mech.* **506**, 79–115.

Shen, L., Zhang, X., Yue, D. K. P. & Triantafyllou, G. S. 1999 The surface layer for free-surface turbulent flows. *J. Fluid Mech.* **386**, 167–212.

Smolentsev, S. & Miraghaie, R. 2005 Study of a free surface in open-channel water flows in the regime from 'weak' to 'strong' turbulence. *Intl J. Multiph. Flow* **31**, 921–939.

Sullivan, P. P. & Patton, E. G. 2008 A highly parallel algorithm for turbulence simulations in planetary boundary layers: Results with meshes up to 1024^3. In *Eighteenth Conference on Boundary Layer and Turbulence*, Stockholm, Sweden, p. 11B.5.

Teixeira, M. A. C. & Belcher, S. E. 2000 Dissipation of shear-free turbulence near boundaries. *J. Fluid Mech.* **422**, 167–191.

Teixeira, M. A. C. & Belcher, S. E. 2002 On the distortion of turbulence by a progressive surface wave. *J. Fluid Mech.* **458**, 229–267.

Teixeira, M. A. C. & Belcher, S. E. 2006 On the initiation of surface waves by turbulent shear flow. *Dyn. Atmos. Oceans* **41**, 1–27.

Tennekes, H. & Lumley, J. L. 1972 . *A First Course in Turbulence*. The MIT press.

Tryggvason, G. 1988 Deformation of a free surface as a result of vortical flows. *Phys. Fluids* **31**, 955–957.

Tsai, W.-T. 1998 A numerical study of the evolution and structure of a turbulent shear layer under a free surface. *J. Fluid Mech.* **354**, 239–276.

Variano, E. A. & Cowen, E. A. 2008 A random-jet-stirred turbulence tank. *J. Fluid Mech.* **604**, 1–32.

Walker, D. T., Leighton, R. I. & Garza-Rios, L. O. 1996 Shear-free turbulence near a flat free surface. *J. Fluid Mech.* **320**, 19–51.

Watanabe, Y., Saeki, H. & Hosking, R. J. 2005 Three-dimensional vortex structures under breaking waves. *J. Fluid Mech.* **545**, 291–328.